

POLITECNICO DI TORINO

Master's Degree in Mechanical Engineering



Master's Degree Thesis

Aerodynamic Forcing Investigations of a Transonic Compressor

Supervisors

Prof. Daniela MISUL

Prof. Simone SALVADORI

Prof. Paolo PENNACCHI

Mr. Nenad GLODIC

Mr. Mauricio GUTIERREZ SALAS

Candidate

Marco CASTALDI

July 2021

Abstract

This thesis aspires to provide a preliminary analysis of unsteady forcing in a transonic compressor. The study and research conducted is placed within the Advanced Research Into Aeromechanical Solutions (ARIAS) project: the experimental test data obtained from the Technische Universität Darmstadt (TUD) compressor test rig are used as a starting point of the work. The report is divided in two macro-sections.

In the first one, a critical pattern of wake generator is taken into account, with staggered blades. This configuration leads to significant stresses and for this reason simulations are necessary to predict possible failures without compromising the experimental setup. The engineering simulation software ANSYS and its packages are used to run the simulations. A preliminary setup is carried out before starting the simulations: this includes the staggered configuration generation with DesignModeler and the creation of the IGV mesh with ICEM CFD. The mesh can be coarse or more refined based on the number of constituent elements and nodes: in order to choose the best mesh, i.e. accurate enough but not too fine, a grid dependence analysis is performed. Three meshes are generated: COARSE, MEDIUM and FINE: for each, a proper y^+ value is chosen by means of an iterative procedure. As a next step, a series of steady state simulations including only the IGV are executed and the MEDIUM mesh has resulted to be a good compromise between accuracy and number of elements. The MEDIUM mesh is then imported in CFX with rotor, stator and OGV, whose meshes in TubroGrid are taken from the ARIAS project literature. To run the correct SS simulation, the compressor operating point at this specific configuration is calculated. Starting from the experimental Campbell diagram, the intersection between the curve related to the third engine order and to the first mode gives the operational speed. The compressor curve is determined by running several SS simulation by varying the outlet static pressure. The intersection with the design line in the TUD pre-tests performance map gives the operating point of the case study. The operating point is obtained also in the case of reference configuration, i.e. no staggered blades, and the results are compared with the case study. Some sensitive differences are found in the blade loading and total pressure, in particular in the wake region and at the rotor leading edge, where shocks are identified.

This pattern serves as a starting point of the work: the aerodynamic forcing of this configuration is not part of this thesis due to limited resources, and it will be built in future studies.

In the second section, two other patterns are considered: the reference one, and an IGV configuration with only staggered blades. The focus is mainly on

the second mode excited by engine order 15 (M2 EO15), and on the fifth mode excited by engine order 30 (M5 EO30). Two transient simulations with the Time Transformation method in CFX are considered with a proper setup. The trend of certain quantities (total pressure, Mach number,...) at the last time step is obtained and some comparisons with the steady state case are carried out. The two cases are compared regarding the excitation force value decomposed in Fourier coefficients. The absolute value of the aerodynamic force is plotted for each Fourier coefficient and some conclusions can be drawn regarding the effect that this force can have on the rotor blades for both cases. This information are useful for future investigations, such as the forced response analysis.

Keywords

CFD, compressor, turbomachinery, steady state, forcing analysis, aerodynamics

Acknowledgements

Working at KTH in collaboration with Politecnico di Torino has been a stimulating and nurturing experience that helped me improve myself and broaden my horizons from the academic viewpoint. This project would not have been possible without the support of many people.

I would like to express my gratitude to my supervisor at KTH, Nenad Glodic: he gave the opportunity to work in the interesting field of aeroelasticity for a semester. He continuously guided and supported me when I had questions and doubts during the work, stimulating my interest and curiosity.

I am also extremely thankful to Mauricio Gutierrez Salas, my co-supervisor at KTH, who gave me constant support with the simulation part. Thanks to his feedbacks and thoughtful tips, I have been able to analyze the topic further and deepen my knowledge in a field I was totally unfamiliar with at the beginning of the year.

Special thanks to Daniela Misul and Simone Salvadori, my dear professors from Politecnico: despite the distance, they followed me throughout my whole year abroad and accepted with pleasure to collaborate with the professors at KTH.

I also thank professor Paolo Pennacchi at Politecnico di Milano for accepting with pleasure the responsibility to supervise me in the framework of Alta Scuola Politecnica Double Degree program. Moreover, I am grateful to Fabian Klausmann and the researchers at TUD for allowing me to use their experimental data and results for my project.

Endless gratitude goes to my family and in particular to my parents, who have always supported me in every day of my study carrier.

This thesis is dedicated to all those that believed in me, especially to my grandmother Rosetta and my granduncle Don Vincenzo who do not live here anymore.

Table of Contents

List of Tables	VI
List of Figures	VII
Acronyms	XI
1 Introduction	1
1.1 Background	2
1.2 Problem	4
1.3 Purpose	4
1.4 Goals	4
1.5 Benefits, Ethics and Sustainability	5
1.6 Methodology	6
1.7 Stakeholders	7
1.8 Delimitations	8
1.9 Outline	8
2 Theoretical Background	9
2.1 General Overview on Issues in Aeromechanics	9
2.2 Unsteady Aerodynamics	13
2.2.1 Forcing Analysis	13
2.3 Computational Fluid Dynamics	15
2.3.1 Fluid Mesh	15
2.3.2 CFX Setup	17
3 Methodology	21
3.1 Simulation Procedure	21
3.2 Geometry - DesignModeler	22
3.3 Mesh - ICEM CFD	22
3.4 CFX	22

4	Setup	23
4.1	Geometry	23
4.2	Mesh Generation	24
4.2.1	Reference case meshing	24
4.2.2	IGV Mesh	24
4.2.3	Meshes after Iterations	24
4.3	Grid Dependence Analysis	28
4.3.1	Post processing and Mesh choice	29
5	Results	41
5.1	Steady State Simulations - Pattern A	41
5.1.1	Operating Point Calculation	41
5.1.2	Results	42
5.2	Steady State Simulations - Pattern B and C	48
5.3	Unsteady Simulations - Patterns B and C	50
5.3.1	Results	50
6	Conclusions and Future Work	55
A	Theoretical Background	57
A.1	Transonic Flow in Axial Compressors	57
A.2	Structural Dynamics in Turbomachinery	59
A.2.1	Free Vibrations	59
A.2.2	Forced Vibrations	60
A.2.3	MDOF Systems	61
A.2.4	Structural Dynamics of Blades and Disks	62
A.3	Forced Response	66
A.4	CFD	67
A.4.1	Governing Equations	67
A.4.2	Turbulence Model	68
B	Additional Information to the Simulations	70
B.1	IGV Meshing with ICEM CFD	70
B.1.1	Blocking Strategy	70
B.1.2	Pre-Mesh	71
B.1.3	Iterative Procedure for the y^+ assessment	76
B.2	CFX Setup - Grid Dependence Analysis	77
B.3	CFX Setup - SS Simulation	80
	Bibliography	82

List of Tables

1.1	Technical Data Darmstadt Transonic Compressor test rig [2]	3
2.1	CFX Mesh Quality Criteria [10]	16
4.1	Mesh Statistics - COARSE mesh	25
4.2	Mesh Statistics - MEDIUM mesh	26
4.3	Mesh Statistics - FINE mesh	26
5.1	Results of the iterative procedure	43
5.2	Operating points for pattern B and C at the new rotational speed (8,681 rpm)	49
A.1	Natural frequencies and normal modes for cantilever beams.	64

List of Figures

1.1	Facility Design of the TUD compressor test rig [2]	3
1.2	Wake Generator Patterns analyzed in this thesis	5
2.1	Triangle of forces by A.R. Collar, 1947 [5]	10
2.2	Illustration of unsteadiness in a turbine stage [6]	11
2.3	Campbell diagram showing frequencies of common aeroelastic problems [8]	12
2.4	Example of density gradient and static pressure for a transonic compressor: two stator rows and one rotor row are shown	14
2.5	Quadrilateral element: <i>ip2</i> (non-orthogonality). Triangular element: <i>ip1</i> (orthogonality) [10]	16
2.6	Schematic representation of the concept behind the Time Transformation Method [12]	19
2.7	<i>Left:</i> Single passage - Time Transformation Model. <i>Right:</i> Two blade passage - Fourier Transformation Model [12]	20
4.1	Reference geometry: IGV, rotor, stator, OGV	23
4.2	IGV Geometry with the staggered blade	24
4.3	IGV Geometry - 5 sectors with staggered central sector	25
4.4	y^+ trend on the blade surfaces - COARSE mesh	26
4.5	y^+ trend on the blade surfaces - MEDIUM mesh	27
4.6	y^+ trend on the blade surfaces - FINE mesh	27
4.7	COARSE mesh main volumes and surfaces	28
4.8	MEDIUM mesh main volumes and surfaces	28
4.9	FINE mesh main volumes and surfaces	28
4.10	Results for COARSE mesh, 10% span, plane at $z = -0.26$	30
4.11	Results for COARSE mesh, 50% span, plane at $z = -0.26$	31
4.12	Results for COARSE mesh, 100% span, plane at $z = -0.26$	32
4.13	Results for MEDIUM mesh, 10% span, plane at $z = -0.26$	33
4.14	Results for MEDIUM mesh, 50% span, plane at $z = -0.26$	34
4.15	Results for MEDIUM mesh, 100% span, plane at $z = -0.26$	35

4.16	Results for FINE mesh, 10% span, plane at $z = -0.26$	36
4.17	Results for FINE mesh, 50% span, plane at $z = -0.26$	37
4.18	Results for FINE mesh, 100% span, plane at $z = -0.26$	38
4.19	Comparison between mesh sizes at 10%, 50% and 90% span, plane at $z = -0.26$	39
4.20	Wake evolution at 50% span at 2 different locations $z = -0.25$ and $z = -0.26$	40
5.1	CFX Setup Geometry	42
5.2	Campbell Diagram TUD compressor [14]	43
5.3	Compressor characteristic curve at $n=17,185$ rpm. The red circle marks the operating point in the staggered configuration. The red line approximately indicates the working line in the TUD pre-tests performance map	44
5.4	Blade Loading and Relative Difference, 50% span	44
5.5	Blade Loading and Relative Difference, 95% span	45
5.6	Mach number, 50% span	45
5.7	Mach number, 95% span	46
5.8	Total pressure, 50% span	46
5.9	Total pressure, 95% span	47
5.10	Density gradient plot on isosurface at 50% span. Shock regions can be clearly identified.	47
5.11	Total pressure, 95% span	48
5.12	Convergence plot relative to the monitor of the torque with respect to the y-axis	49
5.13	Residuals and inlet total pressure at the end of the simulation - Pattern B	51
5.14	Velocity contour plot at 50% span, range 100 m/s-200 m/s	51
5.15	Fourier spectrum: the aerodynamic force contribution is plotted on the y-axis in Newton. On the x-axis, the Fourier coefficient corresponding to the engine orders are shown	52
5.16	Absolute pressure contours at the rotor suction side - EO15. Range: 200 Pa-1,000 Pa	53
5.17	Absolute pressure contours at the rotor suction side - EO30. Range: 0 Pa-300 Pa	54
A.1	Flow patterns in subsonic and transonic flows without boundary layer separation [7]	58
A.2	Normalized coordinate as a function of different values of ζ	60
A.3	Frequency response plots: amplitude (<i>left</i>) and phase (<i>right</i>)	61

A.4	a) Haigh Digram. The green area is the "safe zone" (infinite life). R_m is the UTS (Ultimate Tensile Strength) and $\sigma_w = \sigma_e$ is the endurance limit. The first mode shape (bending) is represented.	
	b) Frequency response amplitude for the SS excitation. D is the damping magnitude. [19]	63
A.5	Fundamental blade vibration modes: first flap mode (<i>left</i>), second flap mode (<i>middle</i>), first torsion mode (<i>right</i>) [20]	64
A.6	Examples of mode shapes of a wheel, +/- indicates the relative phase of the motion in each area, —:deformed shape, ---: undeformed shape, ····: node lines	65
A.7	Natural Frequency vs Nodal Diameter	66
A.8	Nodal diameter modes and wave modes for a blade row.	66
B.1	Blade passage for the non-staggered configuration. Curves, surfaces and points are shown. <i>Yellow</i> : Hub. <i>Gray</i> : Shroud. <i>Blue</i> : Interface. <i>Green</i> : Blade. <i>Purple</i> : Inlet and Outlet	71
B.2	Blade passage for the non-staggered configuration. Curves are shown	71
B.3	Blocking of the reference blade sector	72
B.4	Block topology details: hub and shroud	72
B.5	Block topology details: hub and shroud	73
B.6	Blocking of the staggered blade sector	73
B.7	Block topology details: hub and shroud	73
B.8	Block topology details: hub and shroud	74
B.9	Example of Edge Spacing with N=6 nodes	75
B.10	CFX Setup for grid dependence analysis	79
B.11	Residuals and Total pressure monitoring at the end of a simulation - MEDIUM mesh, SST model	79
B.12	Trends of total pressure and velocity - MEDIUM mesh, SST model, 50% span	80

Acronyms

CFD Computational Fluid Dynamics

ARIAS Advanced Research Into Aeromechanical Solutions

TUD Technische Universität Darmstadt

IGV Inlet Guide Vein

HPC High Pressure Compressor

OGV Outlet Guide Vein

EOs Engine Orders

EO Engine Order

NACA National Advisory Committee for Aeronautics

SS Steady State

ATAG Air Transport Action Group

FEM Finite Element Method

KTH Kungliga Tekniska högskolan

DOF Degree Of Freedom

MDOF Multiple Degrees Of Freedom

UTS Ultimate Tensile Strength

F Flap Mode

E Edgewise Mode

T Torsion Mode

S Stripe Mode

ND Nodal Diameter

ZZENF Zig-Zag shaped Excitation in Nodal diameters versus Frequency

EOMs Equations of Motion

RANS Reynolds Averaged Navier-Stokes

URANS Unsteady Reynolds Averaged Navier Stokes

SST Shear Stress Transport

FEA Finite Element Analysis

GGI General Grid Interface

Chapter 1

Introduction

Sustainability is a topic of immense importance today and it radically influences modern design attitudes, as well as the growth and development of technology. Thinking about the recent advancement in the aerospace sector, a crucial issue is the necessity of new design solutions able to guarantee high efficiency, low noise and positive environmental impacts. One way to reach these goals is to design aircraft engines with fewer stages and thinner sections (blades, vanes, seals). However, this may remarkably increase the load on the components, which are therefore more prone to suffer from vibrations.

Structural vibrations can be considered the major aeroelastic problem in aerospace propulsion, since they can lead to high-cycle fatigue, i.e. the progressive and localized crack growth and propagation which weakens the components and finally leads to failure. This phenomenon occurs suddenly and may cause permanent damage of engine parts, such as rotor/stator blades of the compressor and turbine. Researchers have devoted more attention to the field of aeroelasticity to guarantee reliability in flight safety and control over the operating cost. While focusing on aircraft gas turbine engines, the analysis of the vibrations induced by the flow itself becomes crucial, especially with mixed subsonic-supersonic flows. The nonlinearity and unsteadiness of the transonic dynamic response to the fluid flow makes the problem complex and challenging: several models for aeroelastic stability calculations have been developed. Some methods based on CFD (Computational Fluid Dynamics) have been used to solve unsteady transonic flows [1]. Anyway, numerical simulations should have strong connections with experiments, whose data are fundamental to improve and validate design methods. Neglecting the empirical studies, there is no possibility of enhancement of the current understanding of the physical processes at the root of these vibrations.

In this context, the ARIAS (Advanced Research Into Aeromechanical Solutions)¹ project aims at improving the accuracy of vibration prediction and at investigating the major aeroelastic problems in turbomachinery. This thesis work is placed within the framework of the ARIAS researches, coordinated by the Royal Institute of Technology - KTH (Kungliga Tekniska högskolan). ARIAS was launched on 1 September 2018 and it will be run for a period of four years (48 months). In the next sections of this Chapter, more details will be given about the background of the degree project and the main problems which are addressed, with remarks on its purposes, goals, benefits and stakeholders. The methodologies used in the project are analyzed and its delimitations will be presented. Last but not least, some outlines on the work will be given.

1.1 Background

In this section, a background on this work is provided, with main focus on the ARIAS project. More technical explanation about the theoretical aspects is given in Chapter 2.

The ARIAS project is divided into six work packages: the first one (WP1) aims at understanding and quantifying the compressor forced response and flutter. Experimental measurements are conducted at the TUD (Technische Universität Darmstadt), where researchers study the behaviour of a transonic compressor from an aerodynamic and aeromechanical viewpoint. The data obtained in this phase have been useful for this work, being the input values for CFD simulations. Those simulations help in calculating important variables (such as aerodynamic damping and unsteady pressure) as well as in quantifying uncertainties. At this point, two main concepts should be remarked: first, compressor represents one of the most critical part of an aircraft engine since it constitutes almost half of the engine's length and weight and its vibrations could affect the functionality of the whole system. Second, CFD (Computational Fluid Dynamics) simulations are useful also because they are easier to setup compared to experiments and in a certain sense, they can forecast failure avoiding loss of resources (which may derive from the destruction of the component).

Figure 1.1 depicts the compressor test rig, which is located between the settling chamber and the drive train. The compressor has a modular stage design, i.e. it is divided into smaller *modules* that are: the IGV (Inlet Guide Vein), the rotor, the stator, casing segments and the periphery. Technical details about the rig are given in Table 1.1, in case of single stage compressor setup. This configuration is representative for a HPC (High Pressure Compressor) front stage.

¹For more information: <https://www.arias-project.eu/>

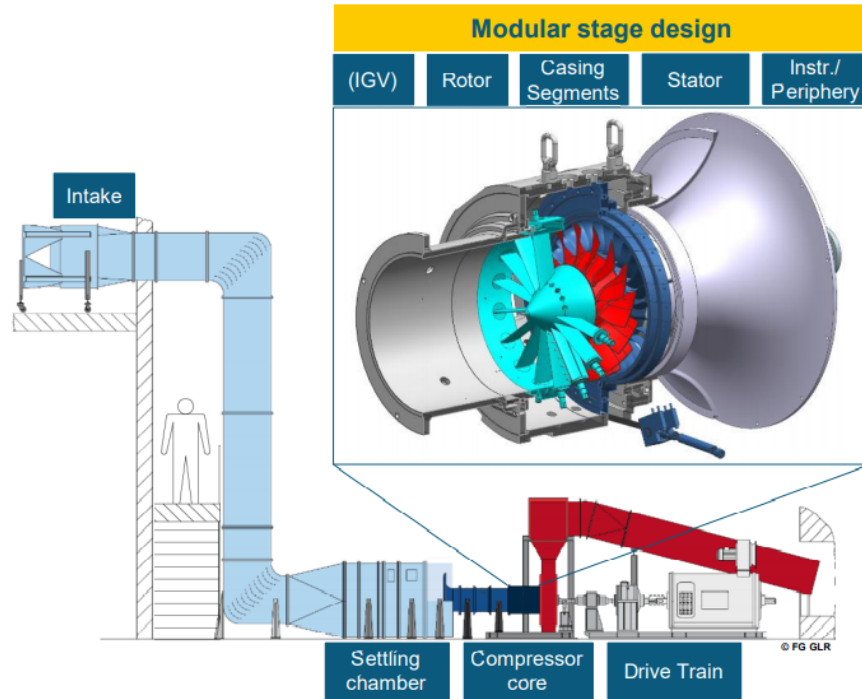


Figure 1.1: Facility Design of the TUD compressor test rig [2]

In/out flow	axial-axial
Electric power	800 kW
Max torque	350 N m
Max speed	21,000 rpm
Max rotor diameter	0.38 m
Hub to tip ratio	≈ 0.5
Relative tip Mach number	1.4
Number blades IGV	3-16
Number blades rotor	16
Number blades stator	29
Number Blades OGV	5

Table 1.1: Technical Data Darmstadt Transonic Compressor test rig [2]

As it is later explained, at TUD a blade aerodynamic forcing due to neighbouring blades is studied, by performing upstream and downstream excitation with different EOs (Engine Orders). Moreover, the influence of excitation features and pattern is considered and attention is devoted on at which extent the tip gap variation

influences synchronous vibrations. The excitation of different EOs is obtained by means of different IGV pattern. Variable NACA (National Advisory Committee for Aeronautics) profiles can be used for the variation of forcing amplitudes. In the next section, the aerodynamic investigation which is at the base of this thesis work will be introduced.

1.2 Problem

The main focus of this written material is three specific configurations (Figure 1.2) of the TUD compressor test rig. The CFD simulations aims at forecasting possible anomalies in the configuration and consequently helping the ARIAS research team to enrich the database of measurements.

Regarding pattern A (Figure 1.2a), it consists in 15 equally-spaced NACA blades, with 3 blades staggered of 20° (Figure 1.2). The reference pattern B (Figure 1.2b) consists in 15 NACA blades, while pattern C (Figure 1.2c) has all the blades staggered of 20° . The focus is on the second mode excited by engine order 15 since it may lead to a critical distribution of aerodynamic forces in some regions of the blade where the mode shape is characterized by high deformation values (e.g. blade tip). Moreover, it is interesting to deepen the influence of the staggered blades at the compressor inlet on the rotor blades: the vibration induced may be troublesome, generate instabilities and critical stress conditions.

1.3 Purpose

The ultimate purpose of this thesis work is to help gaining a broader and deeper understanding of aeromechanics vibrations, in some of its criticalities (in particular aerodynamic forcing excitation). Of course, the research that has been carried out constitutes just one infinitesimal brick of the whole ARIAS activity. From a more practical perspective, this work will help in the creation of a database on complex aeromechanical behaviours that have not been previously investigated. This information will be useful in order to develop new analysis methods, new measurement techniques and new technologies to mitigate harmful vibrations.

1.4 Goals

The final goals of the degree project can be summarized as following:

- Investigation of the patterns explained in Section 1.2 with preliminary activities (geometry and mesh generation).

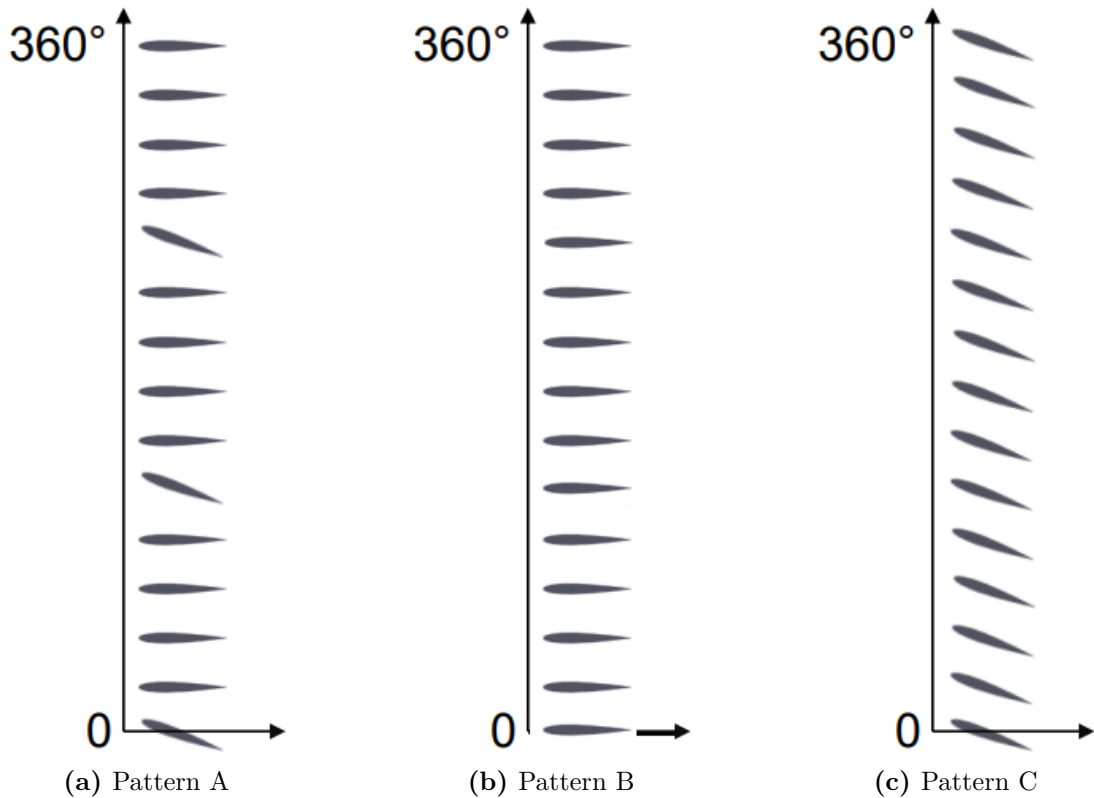


Figure 1.2: Wake Generator Patterns analyzed in this thesis

- SS (Steady State) simulation with calculation of blade loading for pattern A, and comparison with pattern B
- Unsteady aerodynamic study to obtain the excitation force for patterns B and C

1.5 Benefits, Ethics and Sustainability

Nowadays, the aircraft engine manufacturing companies have gained more awareness about the environmental issues and sustainable development has become one of the primary goals in their annual plannings. Supporting institution such as the ATAG (Air Transport Action Group), have been working in tackling climate change as well as improving engine design. Worldwide, flights produced 781 million tonnes of CO₂ in 2015, and aviation is responsible for 12% CO₂ emissions from all transport

sources²: these numbers cannot be neglected and action is urged, especially because aviation is growing fast.

Because of the difficulties in predicting the engine behaviour under vibrations, an over-conservative approach is usually adopted by the manufacturers. This implies higher cost, but especially higher weight and complexity of the component. If there were more knowledge about this topic, lightweight design would help decreasing pollution level and have a positive impact on the environment.

For all these reasons, plenty of institutions and companies may benefit from the researches conducted in the context of the ARIAS project: however, as a first point, it is necessary to underline that everyone can benefit from research, not only related to this field but in general. People's daily life may be improved thanks to these researches and the environment as well. For more details about the stakeholders, i.e. companies and institutions that may have interest and may benefit from the project, refer to section 1.7.

1.6 Methodology

Due to the complexity of the topic from a physical and mathematical point of view, and due to the lack of a full comprehension of the phenomena analyzed within this work, the thesis project does not provide an explanation of the problem that can have general validity. The conclusion which are drawn at the end are not general, but they are still valid to gain more knowledge about unsteadiness and the database can be seen as a starting point of a more structured and rigorous explanation of unsteady aerodynamic forcing. The methodology is therefore both inductive and abductive: some general conclusions are derived for the pattern analyzed at the end: however, one should be aware of their limits. In this research process both numerical and cognitive reasoning has to be combined [3].

This thesis paper deals with the numerical simulations that have been performed to investigate on the pattern in Figure 1.2. Some time has been primarily spent to reproduce the experimental setup in a numerical simulation: a commercial CFD software has been chosen (ANSYS), being very reliable, user-friendly and complete. ANSYS allows to develop both structural analysis (FEM (Finite Element Method)) and CFD simulations. To reduce the computational time and the complexity of the system, some simplifications have been considered, such as including only a significant number of blades instead of the whole empirical domain. After defining the domain, a proper meshing can be obtained by the advanced mesh generation tool ICEM. The simulation are performed with ANSYS CFX for the fluid dynamics analysis. Chapter 3 contains a more detailed description of the problem setup.

²For more information: <https://www.atag.org/>

1.7 Stakeholders

As stated before, many institutions can have interest in the project's outcome. The stakeholders of this project can be identified with the stakeholders of the ARIAS project itself.

It is important to point out that ARIAS has received a funding of 7.5 million € from the Horizon 2020 research and innovation program of the European Union. The stakeholders composing the ARIAS consortium are leading European universities, research centers and aircraft engine industries. The partners are listed below.

- KTH (Sweden)
- GKN Aerospace Sweden AB (Sweden)
- Rolls-Royce PLC (United Kingdom)
- SAFRAN Aircraft Engines (France)
- SAFRAN Helicopter Engines (France)
- SAFRAN Aero Boosters (Belgium)
- Siemens AG (Germany)
- Universidad Politécnica de Madrid (Spain)
- GE Avio SRL (Italy)
- Industria de Turbo Propulsores S.A. (Spain)
- CERFACS (France)
- Università degli Studi di Firenze (Italy)
- Centro de Tecnologías Aeronáuticas (Spain)
- CENAERO (Belgium)
- TUD (Germany)
- Imperial College London (United Kingdom)
- École Centrale de Lyon (France)
- MTU Aero Engines AG (Germany)
- University of Stuttgart (Germany)

1.8 Delimitations

Vibrations can be regarded as such a huge issue in turbomachinery that it would be impossible to completely describe and understand their most intimate influence on the engine behaviour and, consequently, it is hard to derive general design rules from the results in this brief dissertation. Moreover, the results come from the approximations adopted in the numerical model, which should be representative of what happens, but cannot fully replace the experiments and the real physics of the problem. Some reasoning about mesh convergence, plausibility of the results and correctness of the physical and numerical model is introduced in Chapter 3, 4 and 5.

1.9 Outline

The discussion is articulated in several chapters: the first chapter was dedicated to a general introduction, useful to just have an idea of the project. Next chapters dive into the world of aeromechanical vibrations. Chapter 2 presents a theoretical background to the thesis topic, while Chapter 3 focuses on the engineering-related contents, i.e. methods and methodologies more in detail. Chapter 4 deals with the description of the work, starting from the basic models to the characterization of the system in the numerical simulation. Chapter 5 is about results and the related comments. Last but not least, Chapter 6 devotes the attention to the discussion of the whole work and research experience, with some insights on the future studies and perspectives.

Chapter 2

Theoretical Background

In this chapter, a detailed description about the theoretical background of the degree project is presented. It is necessary to remark that the world of aeromechanics is huge, and it is quite difficult to give insights on all its aspects in this dissertation. For this reason, just a general overview on some concepts and issues will be provided: for further information, one can refer to specific publications and/or technical literature presenting the state of the art in a deeper and more complete way. In order to introduce the topics in a more effective way, the chapter is divided into subsection. The first part is devoted to the general classification of aeromechanical problems, while the second one deals with unsteady aerodynamics, focus of the thesis work. Finally, the last part is about CFD. At the end of the Chapter, the reader gains the necessary knowledge to understand the technical contents of next sections. For more details about structural dynamics of turbomachinery components, one can look at Appendix A, which focuses on general aspects in structural dynamics, vibration properties and forced response (A.2-A.3). Besides, some considerations on transonic flow in axial compressors are given (A.1).

2.1 General Overview on Issues in Aeromechanics

The term aeromechanics generally defines the science which is concerned about the motion of gases (especially air) and its effects on bodies in the flow field. The dynamic interaction between fluid and structure is particularly important in some engineering fields, such as aircraft design. One of the branches of aeromechanics is aeroelasticity, defined by Collar as the mutual interaction between aerodynamic, elastic and inertial forces on an elastic structure in a fluid flow field [4]. Figure 2.1 shows this interaction: in particular, two fields can be identified, static aeroelasticity and dynamic aeroelasticity. The former deals with the steady response, the latter

with the dynamic interaction between fluid and structure.

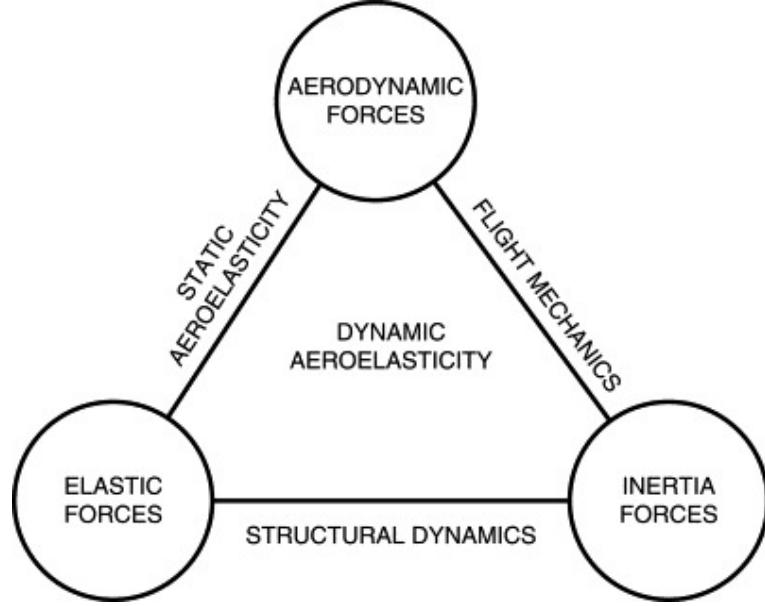


Figure 2.1: Triangle of forces by A.R. Collar, 1947 [5]

Let us now focus on the consequences that vibratory behaviours may have from the aeroelastic viewpoint. In order to perform this analysis, it is convenient to revisit the single DOF (Degree Of Freedom) system with damping. By assuming a general function $F_{ae}(t) = Fe^{i\omega t}$ (aerodynamic force), the solution has general form $x(t) = x_0e^{i\omega t}$, equation A.1 can be written as:

$$(-m\omega^2 + i\omega c + k)x_0e^{i\omega t} = Fe^{i\omega t} \quad (2.1)$$

three forces are balancing the forcing function: inertial force (negative real), damping force (positive imaginary) and elastic force (positive real). The general solution is witnessing a phase lag with respect to the fluid force. If the phase lag is different from 0 and 180°, structural damping is present and the aerodynamic force can be decomposed in an aerodynamic damping force and an aerodynamic elastic force, which can be brought on the left-hand side of equation A.1. The aerodynamic force can be written as sum of aerodynamic disturbance forces and aerodynamic damping forces. The former originates due to several reasons, such as disuniformities in the inlet flow, arrangement of the combustion chamber and presence of adjacent blade rows (wakes from upstream blades and struts). The

latter are caused by the interaction between the blades and the fluid.

$$F_{ae}(t) = F_{damping}(t) + F_{disturbance}(t) \quad (2.2)$$

$$F_{damping}(t) = c_{ae}\dot{x} + k_{ae}x \quad (2.3)$$

$$m\ddot{x} + (c + c_{ae})\dot{x} + (k + k_{ae})x = F_{disturbance}(t) \quad (2.4)$$

If the aerodynamic damping (or simply *aerodamping*) is negative and larger than the structural damping (in absolute value), an instability called *flutter* generates, which occurs close to the natural frequencies of the blade and grows exponentially. Flutter is one the most critical issues in aeromechanics.

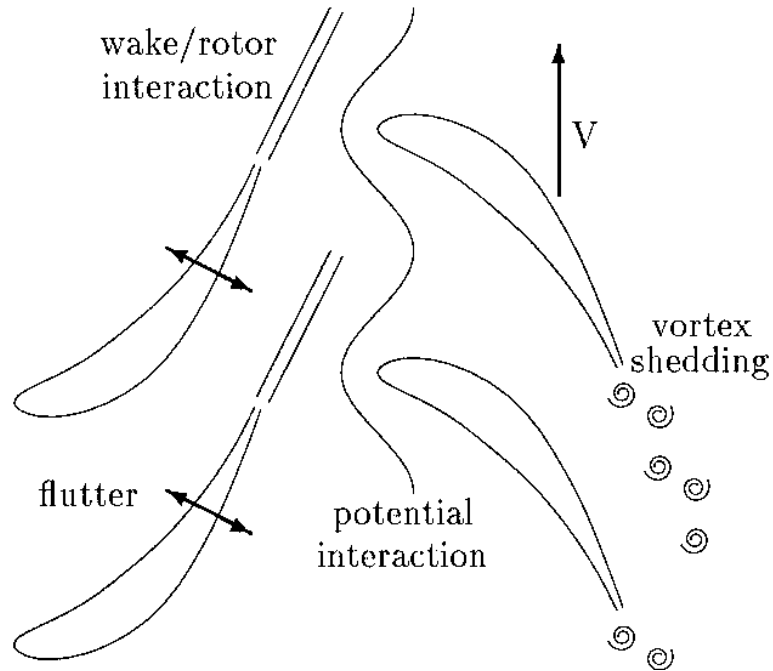


Figure 2.2: Illustration of unsteadiness in a turbine stage [6]

When discussing about aeroelasticity, the unsteadiness can be classified as following [7]:

- Forced Response
- Flutter
- Non-synchronous vibrations
- Separated flow vibrations

Regarding the forced response, it is the vibration induced by aerodynamic disturbance forces in rotors (or stators): the frequencies of these vibrations increase linearly with increasing rotational speed, i.e. at different engine orders (integer multiples of the rotation rate of the rotor). To identify the critical points, the lines corresponding to different engine order are represented in the same plot as the natural frequencies of the component in analysis: this diagram is known as Campbell diagram. In other words, Campbell diagrams are useful to detect when there is a match between (rotor) frequency and mode shape of the excitation and vibration mode shape, which can lead to large forced response. In Figure 2.3 the Campbell diagram is depicted: the natural frequencies of the blades slightly increase with the rotor speed due to centrifugal stiffening [7]. In some cases they might also decrease with the rotor speed due to spin softening. The lines corresponding to different engine orders are plotted as well as the regions where instabilities can occur.

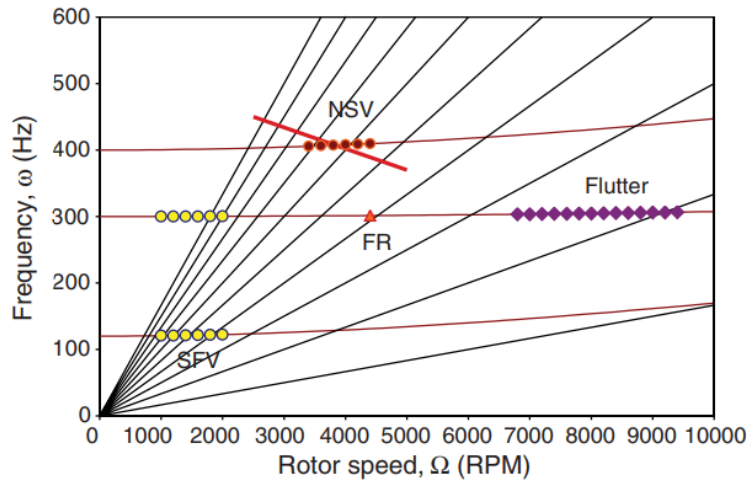


Figure 2.3: Campbell diagram showing frequencies of common aeroelastic problems [8]

Non-synchronous vibrations are caused by vortex shedding, unsteady flow separations and unsteady tip clearance flows. They appear at low-speed off-design conditions. They are non-synchronous since their frequencies are not an integer multiple of the rotor speed. Non-synchronous vibration is frequency-locked, i.e. it begins at a certain frequency and then influences the nearby natural frequencies of the blade, shifting the frequency of the response.

Separated flow vibrations occur at low rotor speed and at off-design conditions with low amplitudes. The causes of these vibrations might be similar to the non-synchronous vibrations, but they do not lock on to close frequencies.

Crossings in the Campbell diagram must be avoided in order to have a safe and reliable design. In the case study of this thesis work, blades and disks in the

rotor can not only vibrate as elastic bodies, but also vibrate due to the presence of the IGV. Let us focus on the latter, i.e. forced response induced in the rotor ($\mathbf{F}_{disturbance}(t)$) by upstream blade passages (IGV).

2.2 Unsteady Aerodynamics

Understanding the leading principles of unsteady aerodynamics is fundamental to look at the results of the simulation in a critical way. The forcing analysis has therefore to be introduced. Insights on the forced response can be found in Section A.3.

2.2.1 Forcing Analysis

To solve for aeroelasticity, the equation of motion 2.4 can be reformulated as:

$$[-M_{str}\omega^2 + C_{str}\omega i + K_{str}]\mathbf{x} = F_{exc} + F_{coupl}(\mathbf{x}) \quad (2.5)$$

As stated before, the forced response is related to the term \mathbf{F}_{exc} (the same as $\mathbf{F}_{disturbance}(t)$), related to the excitation force. The rotor is subject to wakes, potential fields and shocks which result in unsteadiness, i.e. the flow quantities (pressure, velocities,...) change in time following a certain oscillating trend. These variations lead to fluctuations in the blade loading as well. Regarding the torque (product between the blade loading or the pressure of the force impinging the blade and the distance from the shaft), it also changes in presence of an excitation pattern. In case of transient analysis, it can be observed that convergence is reached when the oscillation pattern of flow quantities (such as the pressure) becomes periodic (due to the rotation of the rotor), while in the case of the steady-state, convergence is defined when the flow quantities reach a constant value. Depending on the operating point on the compressor map, a transonic shock can be produced: its impingement on the leading edge can cause unsteadiness. To visualize the shocks, an example is proposed in Figure 2.4, just to show the presence of wakes and shocks at the leading edge due to the upstream rotor. The static pressure plots help identifying potential fields which propagate from the downstream stator (high static pressure) to the rotor.

The stator-rotor interaction depends on the rotational speed of the rotor (synchronous vibrations) and the excitation frequency is a multiple of the rotational speed (depicted in the Campbell diagram as shown in the previous sections). Non-synchronous vibrations are not taken into account in this thesis though their importance in the aeromechanics flow analysis. The pressure field can be represented

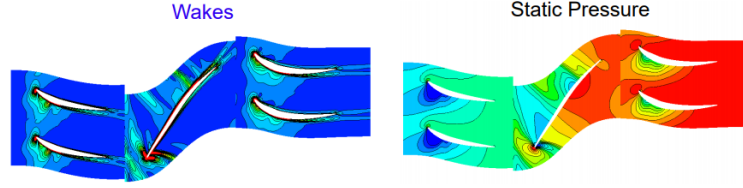


Figure 2.4: Example of density gradient and static pressure for a transonic compressor: two stator rows and one rotor row are shown

as:

$$p(x, y, z, t) = \bar{p}(x, y, z, t) + \hat{p}(x, y, z, t) \quad (2.6)$$

where $\bar{p}(x, y, z, t)$ is the steady part and $\hat{p}(x, y, z, t)$ the unsteady content. The latter can originate from circumferential flow disturbances and can be decomposed in Fourier series in the following way:

$$\hat{p}(x, y, z, t) = p_1(x, y, z) \sin \omega t + p_2(x, y, z) \sin 2\omega t + p_3(x, y, z) \sin 3\omega t + \dots \quad (2.7)$$

Equation 2.6 can be re-written as

$$p(x, y, z, t) = p_0(x, y, z, t) + p_1(x, y, z) \sin \omega t + p_2(x, y, z) \sin 2\omega t + \dots \quad (2.8)$$

Defining Ω the rotor rotational speed (x-axis Campbell diagram), and f the compressor blade frequency (y-axis Campbell diagram), f can be expressed as (in Hertz):

$$f = \frac{\Omega EO}{60} \quad (2.9)$$

where EO indicated the number of flow disturbances (engine orders). From the decomposition of the harmonic content of the excitation force, for each mode (blade passing frequency) both imaginary and real variables are obtained.

Let us briefly mention the ways to reduce the excitation force. One can work in a different region of the Campbell diagram to avoid the resonant point. If this is not possible, the following methods can be used to control the force [9]

- Stacking the blade differently. The stacking can be different from shroud to hub, or from leading edge to trailing edge. Amplitude and phase change accordingly.
- Axial gap between stator and rotor, making the wakes weaker. However, this may lead to an increase in size and weight in the compressor.

- Clocking: choosing different distance from the shaft of the first rotor row and the second one.
- Blade Count Ratio: change the ratio of the number of blades in the stator and in the rotor, keeping pitch-to-chord ratio constant. This results in different modal properties.
- Large Mistuning: force control by mistuning the compressor blades

2.3 Computational Fluid Dynamics

It is very important to understand the physics of the problem before proceeding with the simulations in order to make right assumptions to get both efficiency and accuracy. RANS (Reynolds Averaged Navier-Stokes) equations are chosen for steady-state equations, while URANS (Unsteady Reynolds Averaged Navier Stokes) are used for transient. The turbulence models $k - \varepsilon$ and $k - \omega$ are combined together in the SST (Shear Stress Transport) model, so that the first model is used in the free-shear flow, while $k - \omega$ is implemented in the boundary layer region. For more information regarding governing equations and turbulence models, one can refer to A.4.

2.3.1 Fluid Mesh

The fluid domain is meshed with high quality to have faster convergence and to capture the flow characteristics. In order to correctly solve the boundary layer, the value of y^+ has to be properly chosen.

Mesh Quality

Regarding the mesh quality, mesh orthogonality is a really important concept for the CFX solver. Figure 2.5 shows examples of non-orthogonality and orthogonality for quadrilateral and triangular elements respectively. If the normal vector for each integration point surface n is parallel to the vector joining two control volume nodes s , the mesh orthogonality is of high order. Table 2.1 summarizes CFX mesh quality criteria. Values outside of the suggested acceptable range will increase both sources and the amplification of discretization error. Poor convergence and divergence can be expected under these conditions [10].

y^+ evaluation

To obtain the dimensionless wall distance y^+ , the boundary layer size (wall distance) can be first calculated with the following procedure. The Reynolds number is given

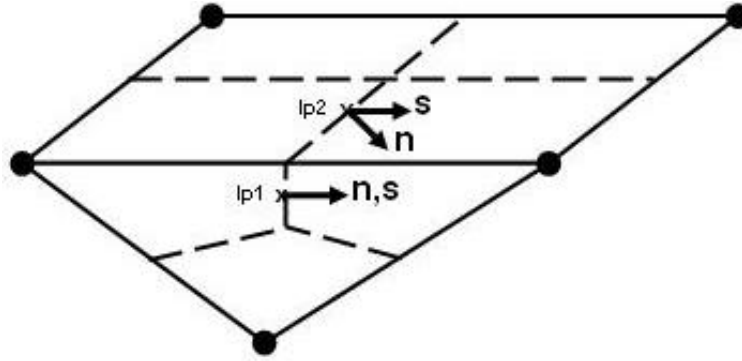


Figure 2.5: Quadrilateral element: *ip2* (non-orthogonality). Triangular element: *ip1* (orthogonality) [10]

Orthogonality Measure and description	Acceptable Range
Orthogonality Angle <i>Area weighted average of $90^\circ - \arccos n \cdot s$ for all integration point surfaces of a control volume</i>	$> 20^\circ$
Orthogonality Factor <i>Area weighted average of $n \cdot s$ associated with each control volume</i>	$> \frac{1}{3}$
Orthogonality Angle Minimum <i>Minimum of $90^\circ - \arccos n \cdot s$ for all integration point surfaces of a control volume. Similar to orthogonality angle, but adverse effects are likely to be less globally significant</i>	$> 10^\circ$
Orthogonality Factor Minimum <i>Minimum of $n \cdot s$ associated with each control volume. Similar to orthogonality factor, but adverse effects are likely to be less globally significant</i>	$> \frac{1}{6}$
Minimum/ Maximum Face Angle (CFD-Post) <i>Minimum/maximum angle between edges of each face that touches a node</i>	$> 10^\circ$ or $< 170^\circ$
Minimum/ Maximum Dihedral Angle(ANSYS ICEM CFD) <i>Minimum/maximum angle between element faces</i>	$> 10^\circ$ or $< 170^\circ$

Table 2.1: CFX Mesh Quality Criteria [10]

by:

$$Re = \frac{\rho U_{FreeStream} L_{BoundaryLayer}}{\mu} \quad (2.10)$$

where ρ is the fluid density, μ the kinematic viscosity, $U_{FreeStream}$ is the characteristic velocity and $L_{BoundaryLayer}$ is the characteristic length scale. The wall shear stress can be defined as

$$\tau_w = C_f \frac{1}{2} \rho U_{FreeStream}^2 \quad (2.11)$$

in which C_f is the skin factor $C_f = 0.027 Re_x^{-1/7}$. The friction velocity is

$$u_* = \sqrt{\frac{\tau_w}{\rho}} \quad (2.12)$$

Finally, the wall distance can be expressed as function of friction velocity:

$$y = \frac{y^+ \mu}{\rho u_*} \quad (2.13)$$

The value of y^+ depends on the turbulence model (SST in this case), on Re number, on Ma number and on fluid flow separation. Best practice is to choose $y^+ < 5$ for the SST model: this value is also reasonable considering viscous dominate flows with separation (as in the analyzed case) [11].

2.3.2 CFX Setup

Obtaining accurate solution in relatively small computational time is one of the main goals of mesh optimization and simulation setup. In this section, CFX setup approaches are introduced, taking into account both SS and transient cases.

Automatic Wall Function

Near the wall, two approaches can be used:

- Wall function: algebraic equations with $k - \varepsilon$ model are implemented to account for the viscous sublayer instead of resolving the boundary layer saving computational resources. This method is limited because when the near wall elements are inside the viscous sublayer ($y^+ < 11.06$), inaccuracy is generated.
- Low-Reynolds-number method solves the boundary layer more accurately but it has higher computational cost.

The Automatic Wall Function is a combination of these two approaches, especially because y^+ is usually hard to predict. If $y^+ > 11.06$, the wall function is used, while if $y^+ < 11.06$ the automatic wall function switches to Low-Reynolds number method.

Mixing Model

The interface between stator and rotor is critical since it controls the transition between a non-rotating component and a rotating one. The mixing models are [10]:

- Frozen Rotor - Steady State: both frames are considered as stationary. Therefore, the model depends on the fixed location of the two frames. A frame transformation is used to represent the rotation of the rotor frame. Because of this flow transformation, the method can be applied when the circumferential variation of the flow is large relative to the component pitch. The Frozen Rotor is the least computationally demanding of the three models, but also provides the lowest accuracy. The model is a good initial guess for Transient Rotor Stator model and also the Stage model in case the mesh has many elements.
- Stage (Mixing plane) - Steady State: the rotor frame is rotating. The flow property fluxes are circumferentially averaged upstream of the interface to obtain the boundary conditions for the downstream component (mixing plane interface). As an effect of the circumferential averaging all transient behavior of the flow is averaged out and the inlet boundary conditions for the downstream interface are steady. This results in higher accuracy for flows with small circumferential variations. The Stage model is more computationally demanding compared to the Frozen Rotor model.
- Transient Rotor Stator (Sliding interface) - Transient: the true transient interaction between components is resolved for maximum accuracy. This is the same method as the Frozen Rotor model but the relative rotation is also taken into account. This model can be used for the same interfaces as used in the Frozen Rotor and Stage models.

Let us define an important concept, the pitch ratio. The pitch ratio is the ratio of the width of the stator blade domain outlet over the rotor blade domain inlet. Scaling the flow with the pitch ratio allows to deal with the unequal pitch ratio in case of Frozen Rotor and Transient Rotor Stator. The unequal pitch is not important for the Stage interface since the fluxes are circumferentially averaged.

Transient Flow Modeling

Modeling the periodic interfaces at the sides of the domain is an essential step to simulate transient flow in a reduced domain, either a single blade passage or a number of passages. Some models require pitch ratio close to unity and a minimum of two blade passages to be modeled. The models included in Transient Blade Row models (CFX) are the following (Figure 2.7):

- Profile Transformation: the signal is shortened or stretched from rotor to stator to deal with unequal pitch problem (which might lead to loss of information in the flow quantities). Useful if the pitch ratio between stator and rotor is close to unity. Not so accurate due to frequency shift at the rotor-stator interface.
- Time Transformation: simulation of a single blade passage. It matches the edges but at a different time step: as shown in Figure 2.6, the same relative position is kept constant from one time step and the next one.

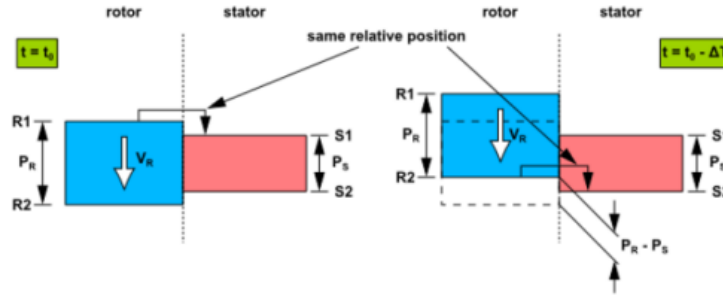


Figure 2.6: Schematic representation of the concept behind the Time Transformation Method [12]

This method can be implemented if the the pitch ratio deviates from unity and is within the range:

$$1 - \frac{M_\omega}{1 - M_\theta} < \frac{P_S}{P_R} < 1 + \frac{M_\omega}{1 + M_\theta}$$

where M_ω is the Mach number associated with the rotor rotational speed, M_θ is the Mach number associated with the rotor rotational speed and P_S and P_R is the pitch of the stator and of the rotor. In most cases, a pitch ratio between 0.9 and 1.1 is accepted. It is useful to define some quantities, which are fundamental while setting up the simulation in ANSYS CFX with the Time Transformation Method:

- Passing Period: time needed to move the blade passage of one pitch:

$$T_s = \frac{60}{n} \frac{1}{N_s} \quad (2.14)$$

where n is the rotational speed in rpm and N_s is the number of blade passages in 360°

- Number of Timesteps per Period: if not enough, the accuracy of the results might be affected (especially the wake), if too many, the computational cost might be too high
- Number of Periods per Run
- Coefficient Loops: number of iterations per time step, which linearize the nonlinearities in the flow equations
- Fourier Transformation: two blade passages have to be modeled to capture the periodicity of the domain. The method consists in the decomposition of the harmonic content of the information coming from the stator. In the rotor, the solver operates in the frequency domain and then the information is translated back to time domain. The model does not have limitation on the pitch ratio.

Time Transformation and Fourier Transformation are based on phase shifted periodic conditions. This means that the rotor and stator sides are periodic boundaries at different instances in time.

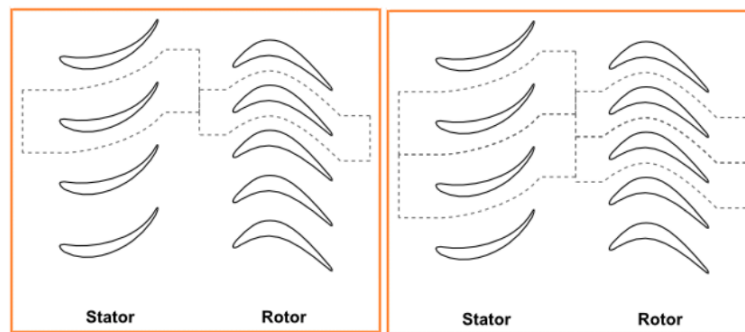


Figure 2.7: *Left:* Single passage - Time Transformation Model. *Right:* Two blade passage - Fourier Transformation Model [12]

Chapter 3

Methodology

In this chapter the methods used to solve the case study are presented, with insight on the engineering simulation software ANSYS: the simulation procedure is first defined, and as a next step some of the packages available in the toolbox of this software are described. This is fundamental to understand the core of the automated process of the simulations and to grasp the basis of the considerations and conclusions drawn in the next chapters¹.

3.1 Simulation Procedure

In this research, the simulation has been carried following certain steps following a logical order. The CFD analysis is carried out using ANSYS 19.2 software.

- Staggered configuration generation with DesignModeler
- Creation of the mesh with ICEM CFD
- Steady state simulation with ANSYS CFX for pattern A (Figure 1.2a)
- Unsteady simulation for forcing using Time Transformation Method with CFX (transient analysis) for patterns B and C (Figures 1.2b-1.2c)

In Chapter 4, the step-by-step work is presented based on the aforementioned points. In this chapter, some generic information is given on the packages: one can refer to ANSYS documentation for more details².

¹For the post processing of the results, Matlab has been used. More information about this software can be found at <https://se.mathworks.com/help/matlab/>

²https://ansyshelp.ansys.com/account/secured?returnurl=/Views/Secured/main_page.html

3.2 Geometry - DesignModeler

DesignModeler is a powerful geometry tool since it allows a good connection between structural and fluid analysis. The blade surfaces are imported from CAD and modified thanks to the different functions provided (*Rotate, Pattern,...*). More than one blade passage can be modeled, and the geometry can then be exported to TurboGrid and to Static Structural to perform FEM assessment.

3.3 Mesh - ICEM CFD

In ICEM CFD a high quality mesh can be created with good control over the mesh fulfilling the criteria defined by the CFX solver. Because the software is thought to mesh existing geometries, it is very hard to import and create geometry. ICEM CFD is much suitable for staggered blades, which might not be meshed in the desired way using TurboGrid. The y^+ value which is calculated from the Re number is used to specify the wall distance of the near wall elements. This, along with the right turbulence model, ensures that the boundary layers are well resolved.

3.4 CFX

The software CFX is used to simulate the fluid behavior in the turbine. It offers a specific setup approach for turbomachines to make the set up procedure simpler. Both steady state and transient simulations are performed in CFX. It offers a wide variety of turbulence models and boundary conditions settings. Periodic boundary conditions are needed to simulate the SBP. For the steady simulation the mesh ensures the periodicity. What goes out of one boundary cell goes into the next one on the opposite side. This is called rotational general connection in CFX. For the transient simulation a more advanced method is needed to ensure the transient behavior of the flow. For the lowest computational time and because of the unequal pitch ratio between components the Time Transformation modeling is used. In the next chapters, more details will be provided specifically regarding the research case analyzed in this thesis work.

Chapter 4

Setup

The setup phase is the core of any simulation activity: starting from the geometry of the case study, a mesh has to be generated in order to guarantee the correct discretization of the problem. The mesh can be coarse or more refined based on the number of constituent elements (and nodes): in order to choose the best mesh (accurate enough but not too fine) a grid dependence analysis can be performed. Let us go through the setup steps before running the steady and unsteady analyses.

4.1 Geometry

In Figure 4.1 the geometry corresponding to the reference case is depicted. The IGV blades are all not staggered and therefore the system can be simulated in a simplified way by considering only one blade. On the other hand, Figure 4.2 shows the IGV with the staggered pattern: 5 blades obtained by rotation of 24° of an initial blade. The central staggered blade is obtained by tilting the original blade of 20° along the tilting axis (from experimental setup).

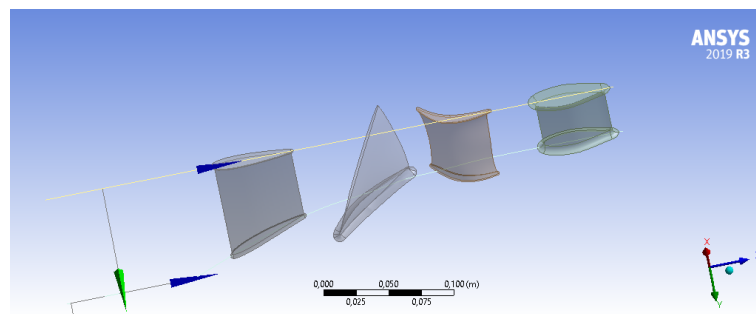


Figure 4.1: Reference geometry: IGV, rotor, stator, OGV

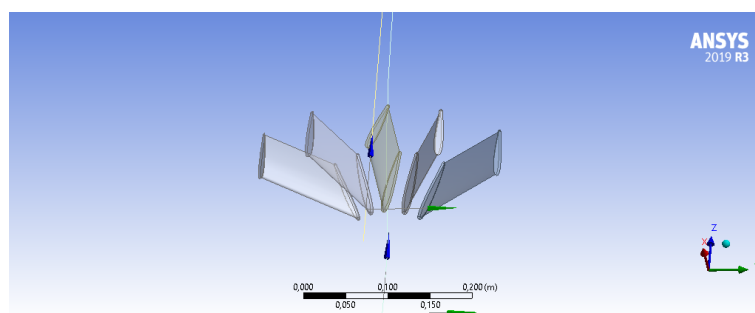


Figure 4.2: IGV Geometry with the staggered blade

4.2 Mesh Generation

Regarding the meshing of the rotor, stator and OGV, the automatic mesh generation is implemented with TurboGrid. However, for the IGV, ICEM CFD is used in order to correctly mesh the staggered blade. For more information about the blocking and pre-mesh, one can look at Appendix B (B.1).

4.2.1 Reference case meshing

Let us briefly present the mesh statistics of the components meshed with TurboGrid. To notice that scope of this thesis is also to acquire familiarity with ICEM CFD, a much more advanced software than TurboGrid. The meshes of rotor, stator and OGV are taken from the literature of the ARIAS project [13].

- Rotor (0.8 mm tip clearance): 1318912 nodes, 1275134 elements (single blade passage)
- Stator: 729648 nodes, 698232 elements (single blade passage)
- OGV: 962605 nodes, 927168 elements (single blade passage)

4.2.2 IGV Mesh

Different meshes are generated based on three refinement levels: COARSE, MEDIUM and FINE. An iterative procedure to calculate the correct y^+ value is implemented to obtain the optimal mesh statistics (B.1).

4.2.3 Meshes after Iterations

The mesh generated for the single reference sector is rotated 3 times to obtain the other 3 sectors. The central staggered sector is added as a next step. The geometry

of the 5 sectors together is shown in Figure 4.3. The mesh can have different levels of refinement: COARSE, MEDIUM and FINE. Appendix B contains explanation of the parameters introduced in the mesh statistics (quality, determinant,...).

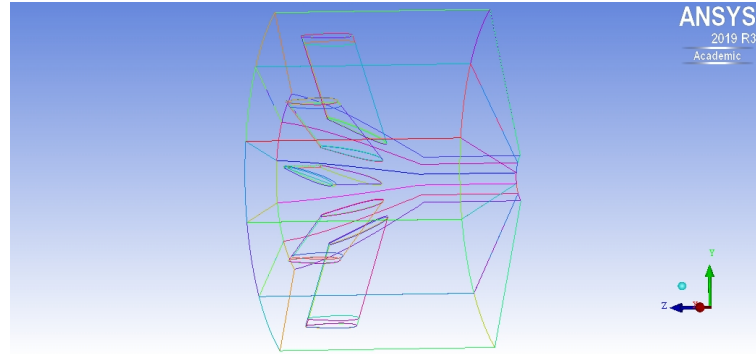


Figure 4.3: IGV Geometry - 5 sectors with staggered central sector

For the COARSE mesh, the results are schematized in Table 4.1 and Figure 4.4: as it can be seen, the highest y^+ is at the leading edge, where the fluid impinges. Here, the viscous effects are still dominant, but turbulent flow is larger with respect to the other two mesh options.

Domain	Number of Nodes	Minimum Angle	Minimum Determinant 3x3x3	Minimum Quality	Maximum Aspect Ratio	Maximum y^+
Reference Sector	112400	20.16°	0.555	0.345	4760	-
Staggered Sector	121640	20.34°	0.682	0.348	7240	-
Total	571240	-	-	-	-	4.766

Table 4.1: Mesh Statistics - COARSE mesh

For the MEDIUM mesh, the results are schematized in Table 4.2 and Figure 4.5: the highest y^+ is still at the leading edge, and the regions with higher y^+ are in low-span regions (close to the hub). This value of local Reynolds number is more suitable to flows with separation.

For the FINE mesh, the results are schematized in Table 4.3 and Figure 4.6: the highest y^+ is still at the leading edge, and the regions with higher y^+ are in low-span regions (close to the hub). A finer discretization allows to decrease the maximum y^+ value, which is located in a smaller region of the blade.

Figures 4.7-4.8-4.9 show some critical mesh and volume surfaces. As best practice, the two interfaces should have similar mesh resolution on both sides and

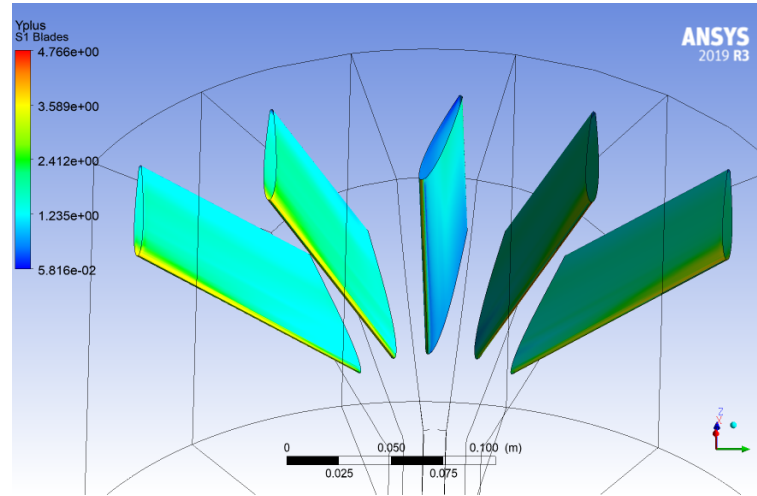


Figure 4.4: y^+ trend on the blade surfaces - COARSE mesh

Domain	Number of Nodes	Minimum Angle	Minimum Determinant 3x3x3	Minimum Quality	Maximum Aspect Ratio	Maximum y^+
Reference Sector	295200	20.34°	0.61	0.348	16500	-
Staggered Sector	295200	20.25°	0.768	0.347	15100	-
Total	1476000	-	-	-	-	2.496

Table 4.2: Mesh Statistics - MEDIUM mesh

Domain	Number of Nodes	Minimum Angle	Minimum Determinant 3x3x3	Minimum Quality	Maximum Aspect Ratio	Maximum y^+
Reference Sector	509280	20.43°	0.812	0.35	18500	-
Staggered Sector	509280	20.25°	0.768	0.347	15400	-
Total	2546400	-	-	-	-	1.090

Table 4.3: Mesh Statistics - FINE mesh

the separation gap should be smaller than the local mesh resolution. The interface between different sectors can be 1:1 or GGI (General Grid Interface). Because the sectors with straight blade are obtained from each other by rotation, at the interface between 2 straight blade sectors 1:1 connection will be applied (no overlap regions), while at the interface between straight and staggered blade sector, GGI

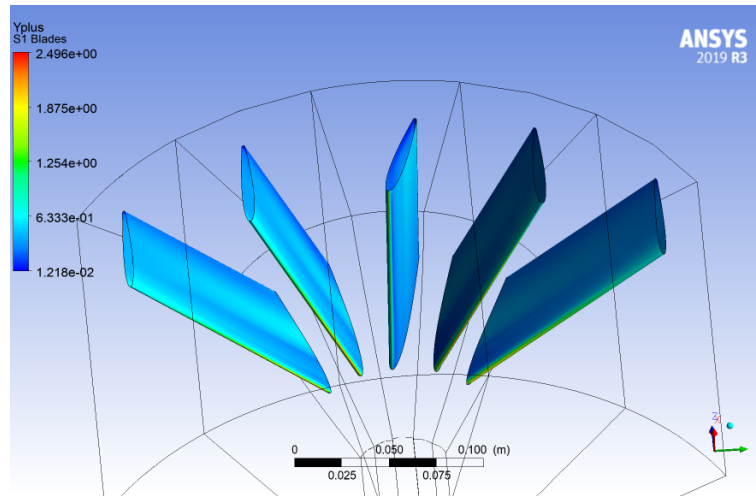


Figure 4.5: y^+ trend on the blade surfaces - MEDIUM mesh

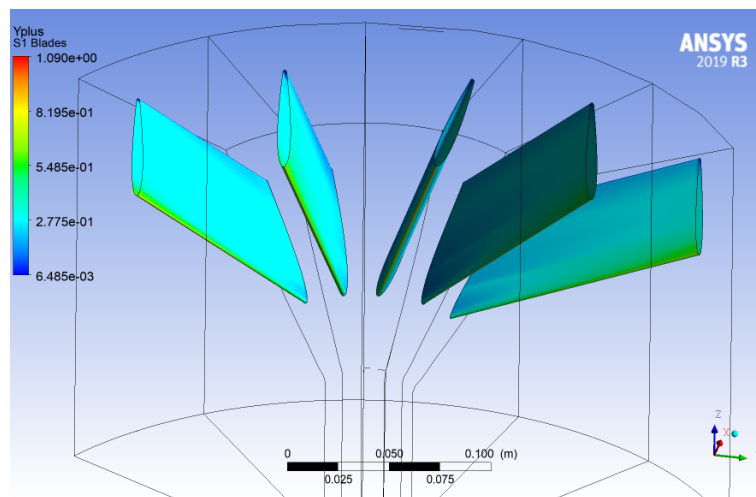


Figure 4.6: y^+ trend on the blade surfaces - FINE mesh

interface is more appropriate, since the matching has been done manually and there could be some small overlap regions (with non-overlap region areas of the order maximum 10^{-3} and minimum 10^{-9}). If one sets *Automatic* in the CFX *Interface* definition under the voice *Mesh Connection*, CFX will automatically identify the regions in which 1:1 connection can be applied and vice versa. GGI interface has to be set when dealing with stator-rotor interfaces.

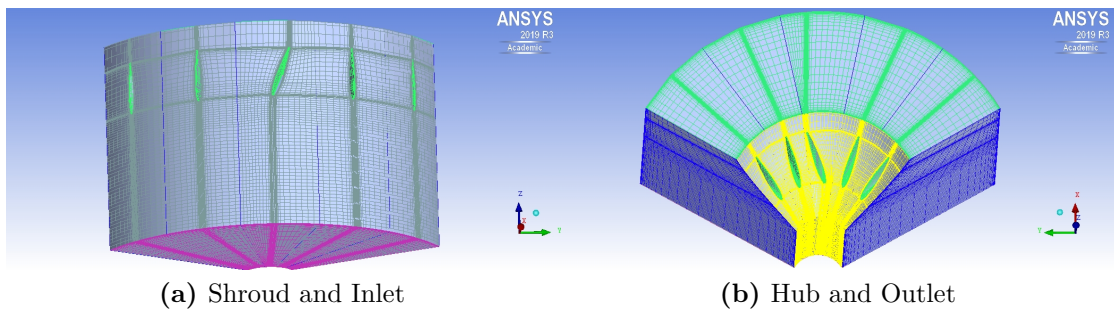


Figure 4.7: COARSE mesh main volumes and surfaces

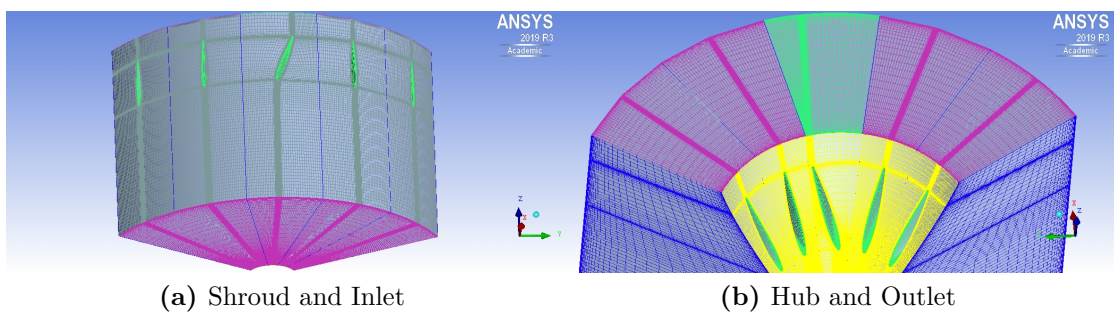


Figure 4.8: MEDIUM mesh main volumes and surfaces

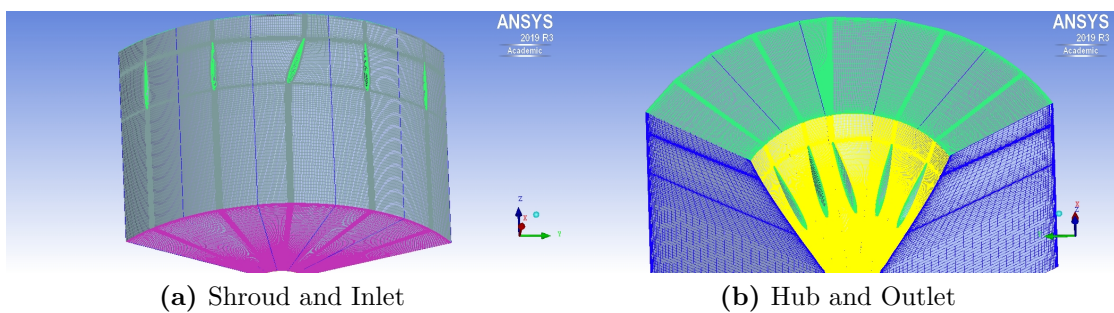


Figure 4.9: FINE mesh main volumes and surfaces

4.3 Grid Dependence Analysis

To perform the grid dependence analysis, a series of simulations can be run, taking into account three different models: $k - \varepsilon$, $k - \omega$ and SST. For each mesh, three different simulations are computed and the results are post processed to underline the strengths and weaknesses of each model. For the CFX Setup of these simulations,

refer to Section B.2.

4.3.1 Post processing and Mesh choice

In CFX-Post the results can be analyzed regarding the wake change while getting closer to the outlet (creation of xy planes at different z-coordinate): the differences between the turbulent models are also analyzed. Every result can be evaluated at several span levels: for simplicity, just the results at 10%, 50% and 90% are shown. The data from CFX are post-processed in Matlab. Let us define p_{SST}^0 the total pressure at the IGV outlet calculated with the SST model, and $p_{k\varepsilon}^0$ and $p_{k-\omega}^0$ the same variable computed with $k - \varepsilon$ and $k - \omega$ respectively. The difference d_1 between SST and $k - \varepsilon$ is obtained in the following way:

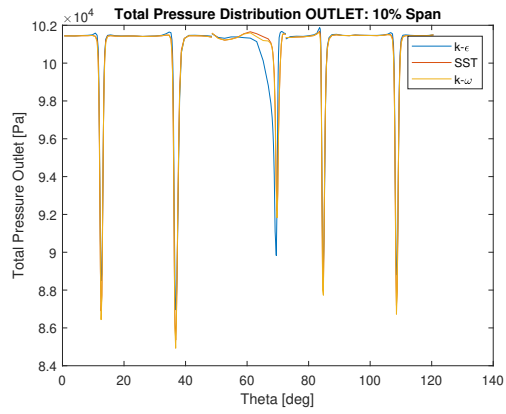
$$d_1 = \frac{|p_{SST}^0 - p_{k\varepsilon}^0|}{p_{SST}^0}$$

while the difference d_2 between SST and $k - \omega$ is computed as

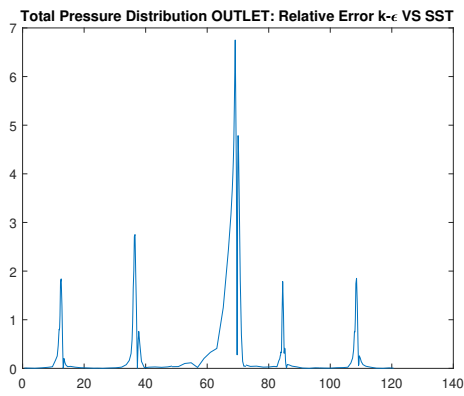
$$d_2 = \frac{|p_{SST}^0 - p_{k\omega}^0|}{p_{SST}^0}$$

COARSE

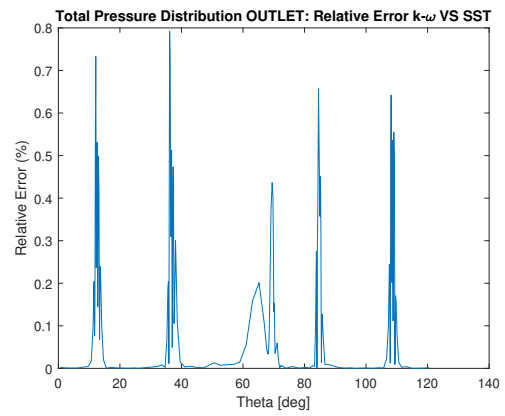
From Figures 4.10-4.11-4.12, it can be concluded that $k - \varepsilon$ model is less accurate in the prediction of the wake losses (especially the one referred to the staggered blade). On the other hand, $k - \omega$ and SST are quite close, even though the relative difference increases with the span (maximum difference is approximately 0.8% for 10% span, 2% for 50% span and 5% for 100% span) and it is maximum when the pressure dip is maximum. As expected, the difference between $k - \omega$ and SST tends to increase far from the blades ($k - \omega$ is not accurate in the free stream), while the difference between $k - \varepsilon$ and SST decreases. The pressure losses are higher towards the shroud. However, due to the high value of y^+ at the leading edge, the boundary layer is not resolved with high accuracy: for this reason, a comparison with the other two meshes has to be carried out.



(a) Comparison $k - \epsilon$, $k - \omega$ and SST

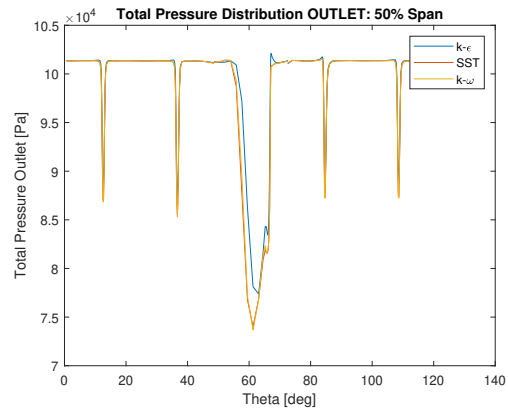


(b) Relative Difference $k - \epsilon$ vs SST

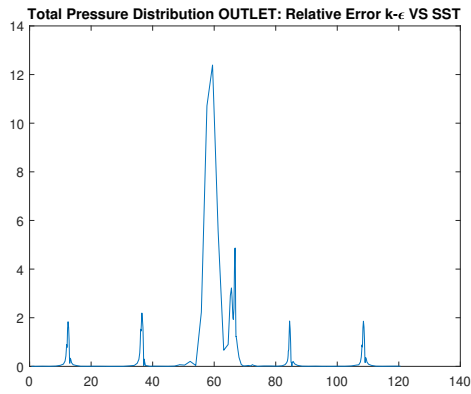


(c) Relative Difference $k - \omega$ vs SST

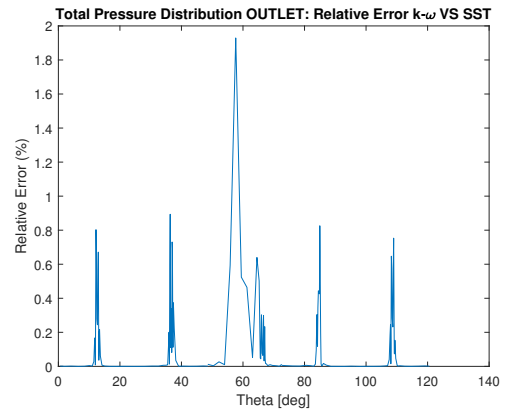
Figure 4.10: Results for COARSE mesh, 10% span, plane at $z = -0.26$



(a) Comparison $k - \epsilon$, $k - \omega$ and SST

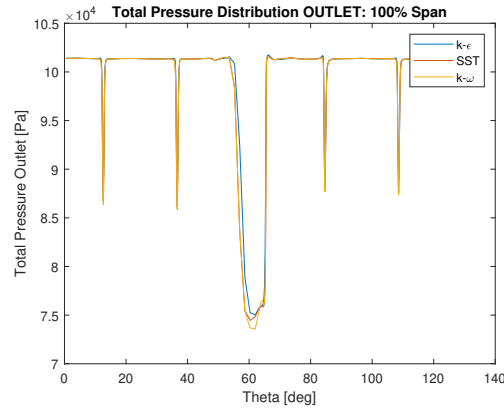
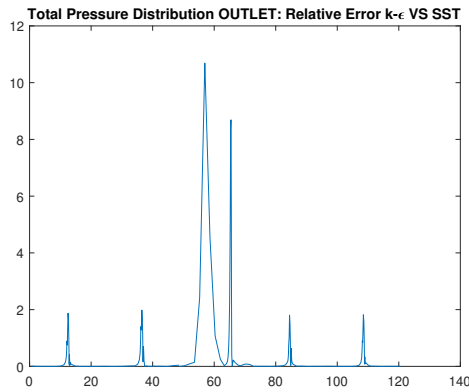
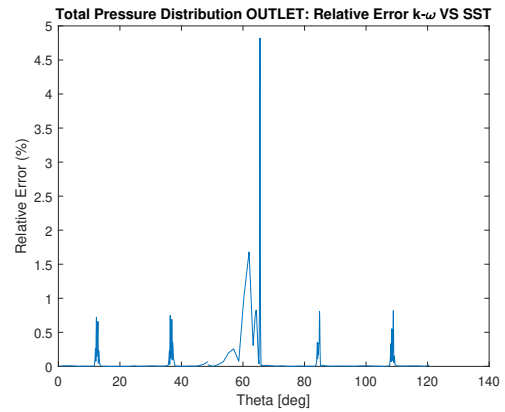


(b) Relative Difference $k - \epsilon$ vs SST



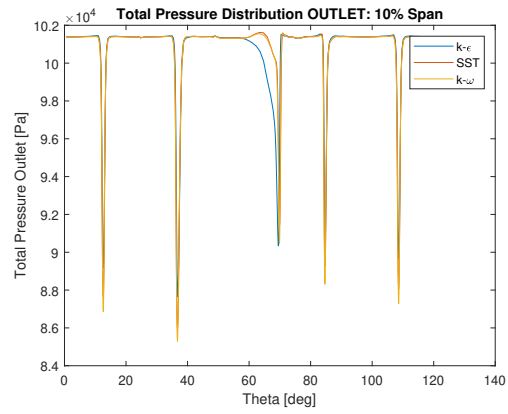
(c) Relative Difference $k - \omega$ vs SST

Figure 4.11: Results for COARSE mesh, 50% span, plane at $z = -0.26$

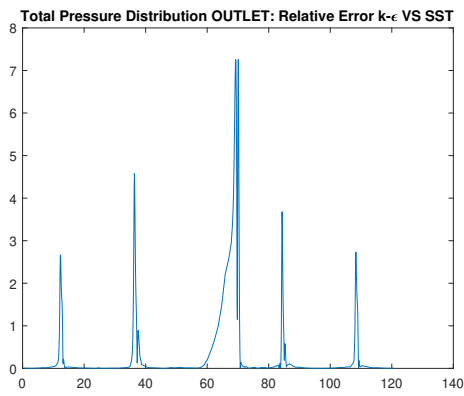
(a) Comparison $k - \epsilon$, $k - \omega$ and SST(b) Relative Difference $k - \epsilon$ vs SST(c) Relative Difference $k - \omega$ vs SST**Figure 4.12:** Results for COARSE mesh, 100% span, plane at $z = -0.26$

MEDIUM

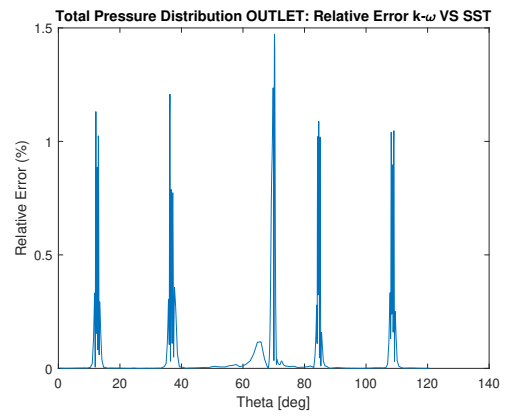
The considerations that can be done for the MEDIUM mesh are the same as for COARSE mesh (Figures 4.13-4.14-4.15). The relative error between $k - \omega$ and SST increases with the span (maximum error is approximately 1.5% for 10% span, 2.5% for 50% span and 4.5% for 100% span) and it is maximum when the pressure dip is maximum. Being the y^+ value smaller compared to the COARSE mesh, as expected the difference between SST and $k - \epsilon$ is also higher for the wakes corresponding to the straight blades. Increasing the span, the wakes become wider (higher pressure losses) and also the difference between SST and $k - \omega$ is higher, especially for the staggered blade. This suggests that there are some discrepancies in the near-wall regions where fluid flow separation happens.



(a) Comparison $k - \epsilon$, $k - \omega$ and SST

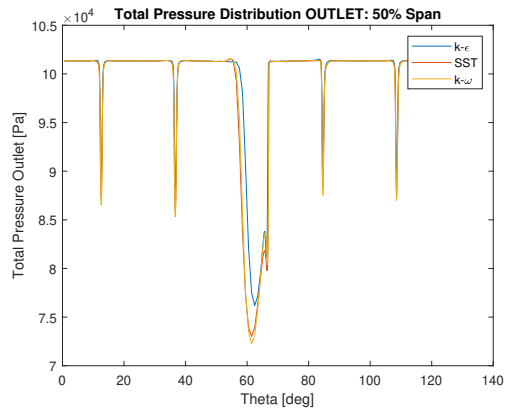


(b) Relative Difference $k - \epsilon$ vs SST

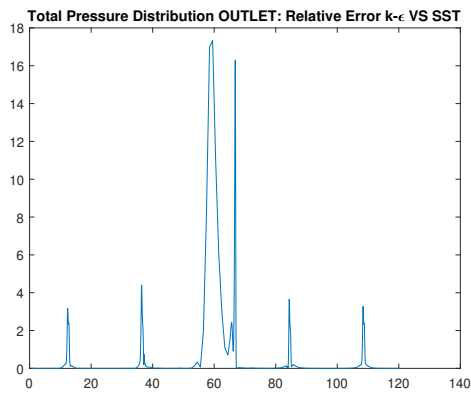


(c) Relative Difference $k - \omega$ vs SST

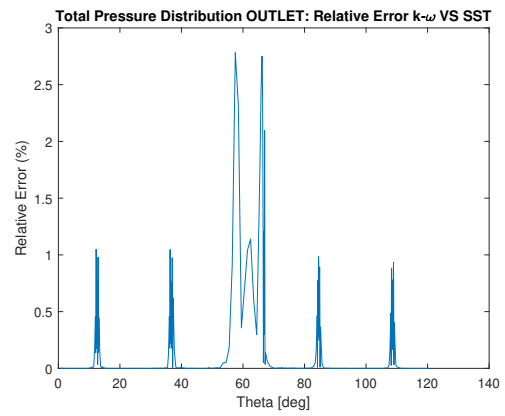
Figure 4.13: Results for MEDIUM mesh, 10% span, plane at $z = -0.26$



(a) Comparison $k - \epsilon$, $k - \omega$ and SST

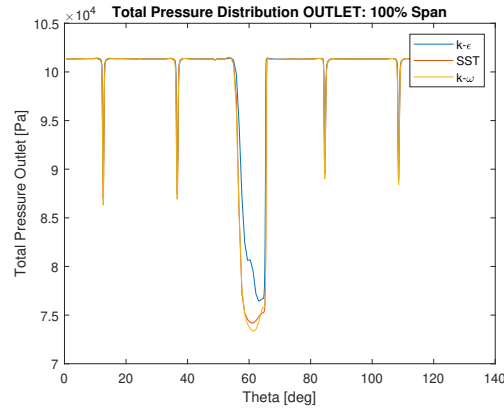
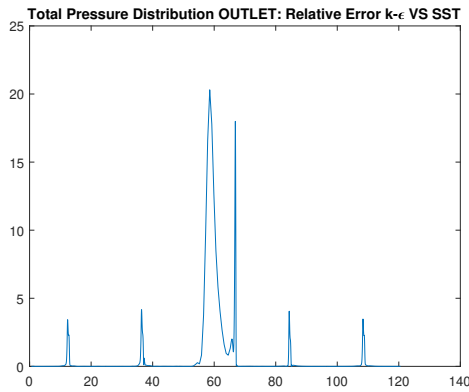
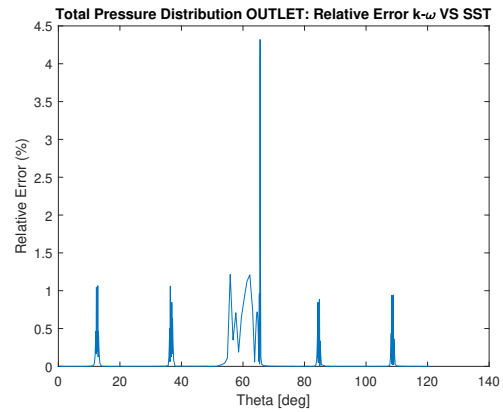


(b) Relative Difference $k - \epsilon$ vs SST



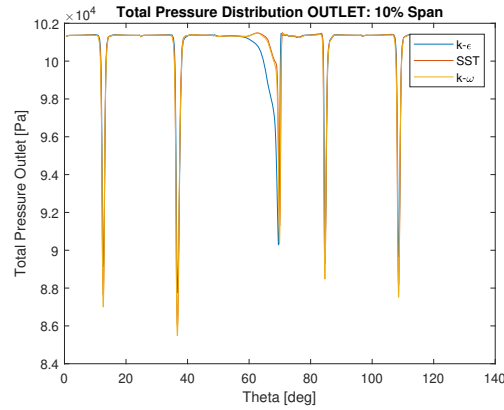
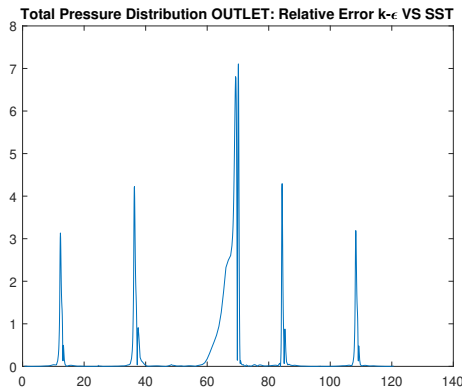
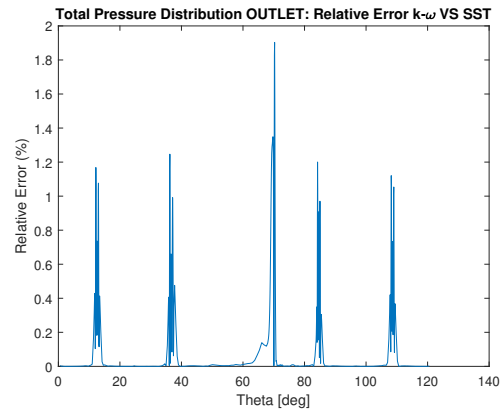
(c) Relative Difference $k - \omega$ vs SST

Figure 4.14: Results for MEDIUM mesh, 50% span, plane at $z = -0.26$

(a) Comparison $k - \epsilon$, $k - \omega$ and SST(b) Relative Difference $k - \epsilon$ vs SST(c) Relative Difference $k - \omega$ vs SST**Figure 4.15:** Results for MEDIUM mesh, 100% span, plane at $z = -0.26$

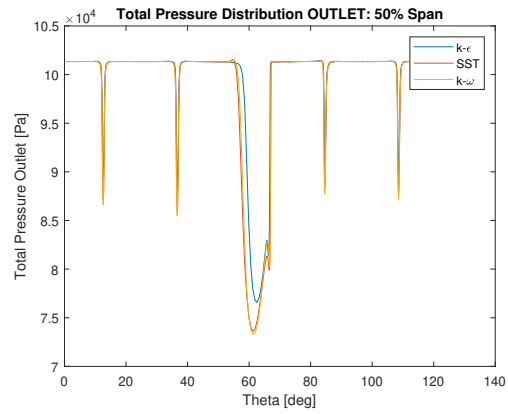
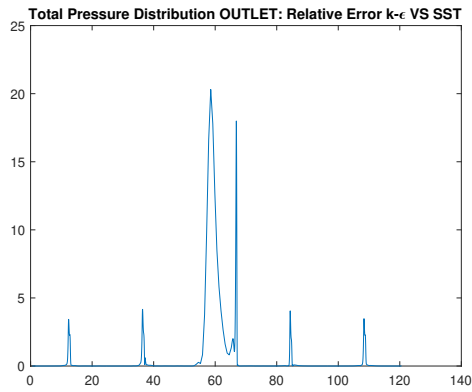
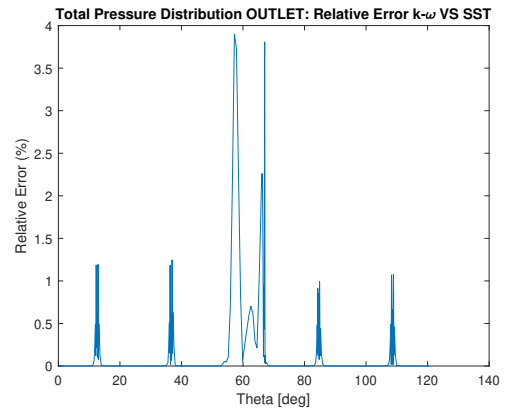
FINE

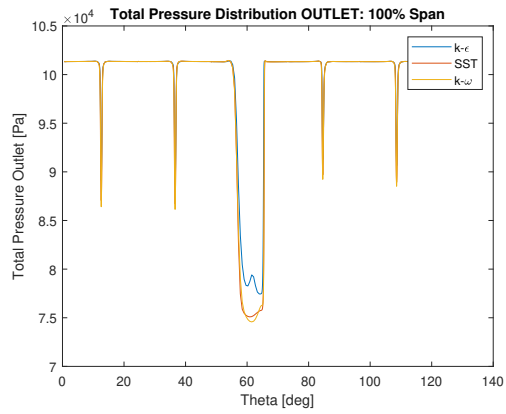
The considerations that can be done for the FINE mesh are the same as for COARSE and MEDIUM mesh (Figures 4.16-4.17-4.18), and as in the previous cases the relative difference between $k - \omega$ and SST increases with the span (approximately 1.9% for 10% span, 4% for 50% span and 5% for 100% span) and it is maximum when the pressure dip is maximum. The plots of the difference between SST and $k - \epsilon$ model shows even higher discrepancies. It is interesting to notice that the differences of trend from hub to shroud are influenced by the different y^+ distribution. In some areas, the y^+ is close to unity and then it starts to decrease along the blade leading edge: this influences the level of detail with which the flow separation is solved.

(a) Comparison $k - \epsilon$, $k - \omega$ and SST(b) Relative Difference $k - \epsilon$ vs SST(c) Relative Difference $k - \omega$ vs SST**Figure 4.16:** Results for FINE mesh, 10% span, plane at $z = -0.26$

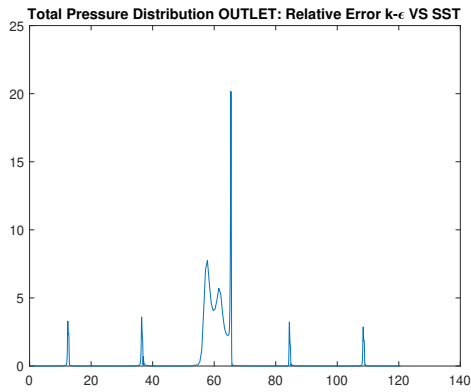
In Figure 4.19, COARSE, MEDIUM and FINE meshes are compared. The COARSE mesh slightly overestimates the pressure minima corresponding to the straight blades, while underestimates the intensity of the wake generated by the staggered blade. MEDIUM and FINE show very close results: the best mesh choice is the MEDIUM since having a too fine mesh would considerably increase the computation cost, especially when running transient simulation with the other components (rotor,...).

Another interesting aspect one can evaluate is the change of the wake as a function of the plane location. The wake evolves while getting closer to the outlet. The results for the three types of meshes are summarized in Figure 4.20. As it can be seen, the wake intensity decreases as expected.

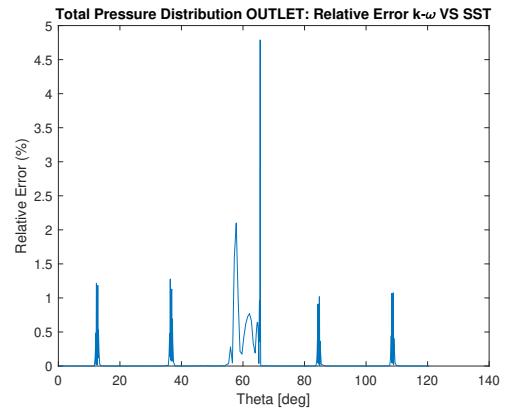
(a) Comparison $k - \epsilon$, $k - \omega$ and SST(b) Relative Difference $k - \epsilon$ vs SST(c) Relative Difference $k - \omega$ vs SST**Figure 4.17:** Results for FINE mesh, 50% span, plane at $z = -0.26$



(a) Comparison $k - \epsilon$, $k - \omega$ and SST

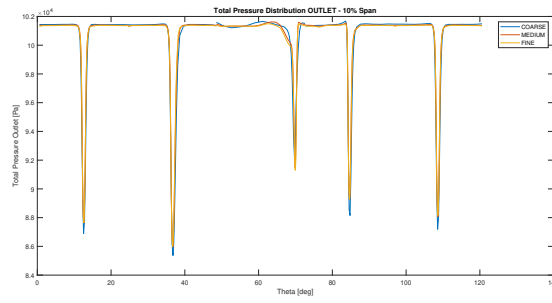


(b) Relative Difference $k - \epsilon$ vs SST

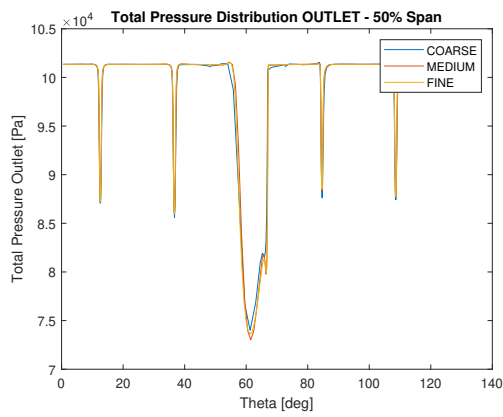


(c) Relative Difference $k - \omega$ vs SST

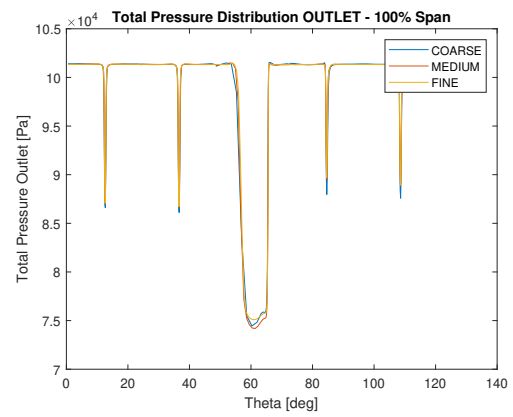
Figure 4.18: Results for FINE mesh, 100% span, plane at $z = -0.26$



(a) 10% span



(b) 50% span



(c) 190% span

Figure 4.19: Comparison between mesh sizes at 10%, 50% and 90% span, plane at $z = -0.26$

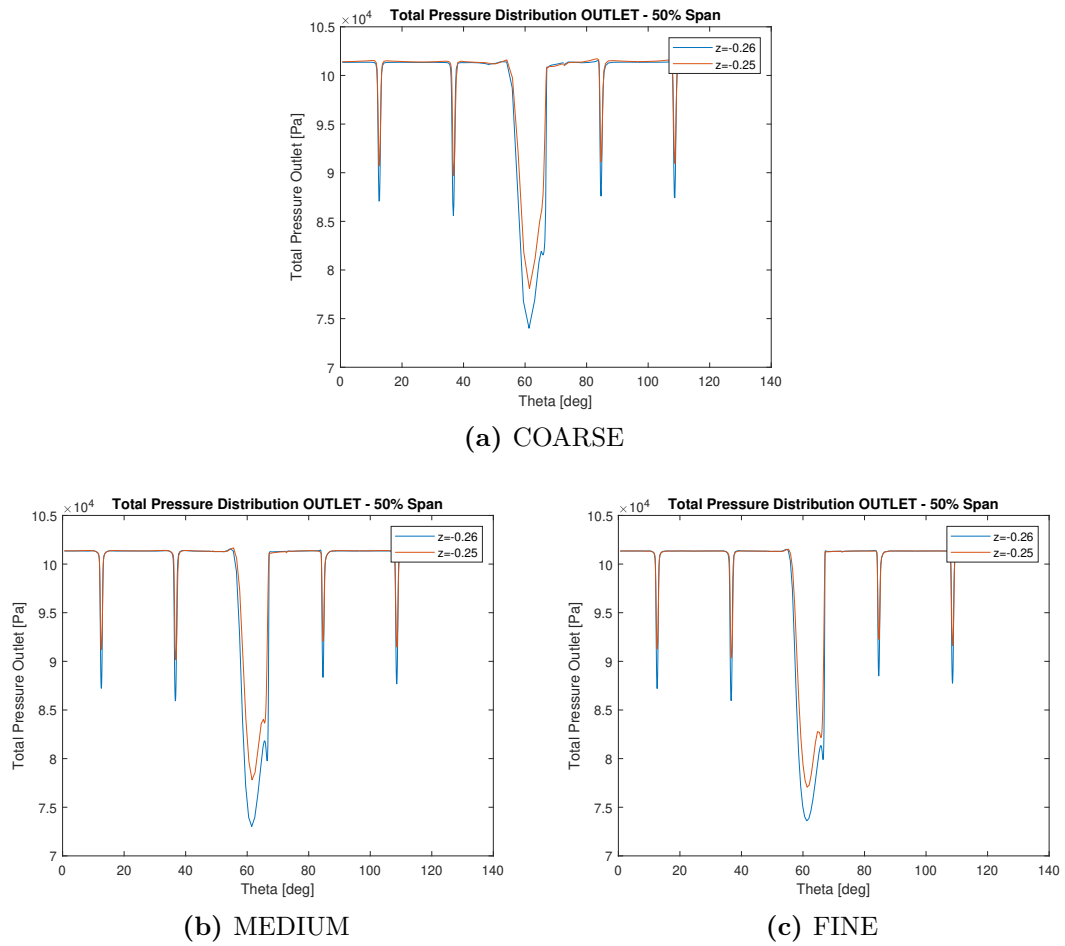


Figure 4.20: Wake evolution at 50% span at 2 different locations $z = -0.25$ and $z = -0.26$

Chapter 5

Results

After the preliminary activities, the steady state and transient simulations are carried out. When the rotor, stator and OGV are included, the computation time is likely to remarkably increase. The chosen mesh for the IGV is the MEDIUM one. The reference case simulation is considered as well, with just one straight blade to model the IGV. More information about setup and results is given in the following sections.

5.1 Steady State Simulations - Pattern A

5.1.1 Operating Point Calculation

In Figure 5.1 the 2 geometries are shown. The features of each are summarized as following:

1. Reference SS (pattern B):
 - IGV: 15 straight vanes (pitch angle 24°)
 - Rotor: 16 blades (pitch angle 22.5°)
 - Stator: 29 vanes (pitch angle 12.414°)
 - OGV: 5 vanes (pitch angle 72°)
2. Pattern A: 5 IGV passages are modeled, therefore considered as a unique solid with pitch angle of 120° when defining the interface stator-rotor. The system is not fully periodic.
 - IGV: 15 vanes with 3 staggered blades (pitch angle 24°)
 - Rotor: 16 blades (pitch angle 22.5°)

- Stator: 29 vanes (pitch angle 12.414°)
- OGV: 5 vanes (pitch angle 72°)

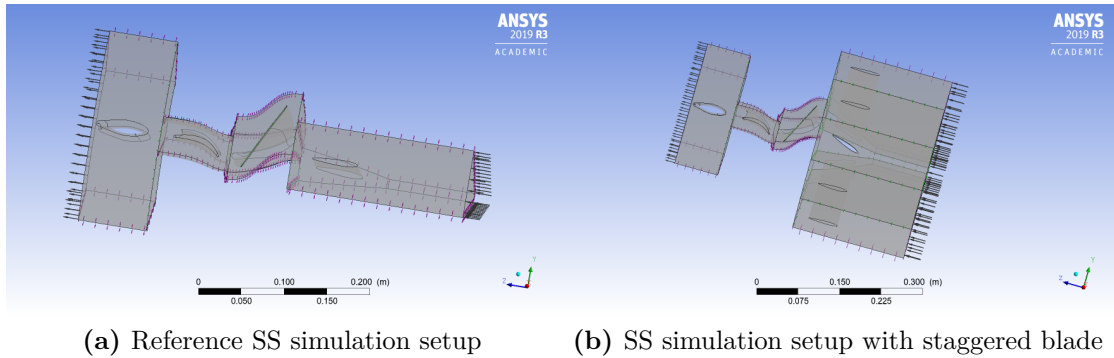


Figure 5.1: CFX Setup Geometry

The setup for the IGV is similar to the one done for the grid dependence analysis, but the rotational speed has to be calculated beforehand. For this pattern, the crossing between the first mode and the third engine order excitation has been chosen. The steady state results derived from these simulations will be useful for the unsteady forcing analysis that will be carried out outside of the present work.

From the experimental Campbell diagram (Figure 5.2), this speed is 17,185 rpm, corresponding to a rotor blade frequency of around 859.25 Hz. The compressor curve has to be determined by running several SS simulation at 17,185 rpm and varying the outlet static pressure. The intersection with the design line in the TUD pre-tests performance map will give the operating point of the case study.

The main information about the iterations is shown in Table 5.1, where the row in bold refers to the operating point.

For pattern B, the operating point has the following output variables:

$$\text{Outlet Total Pressure} = 132,568 \text{ Pa}$$

$$\text{Pressure Ratio} = 1.308$$

$$\text{Mass Flow Rate} = 14.13 \text{ kg/s}$$

In Figure 5.3 the characteristic curve is shown and the operating point is underlined.

Appendix B contains details on the setup of the SS simulation at the operating point of interest (B.3).

5.1.2 Results

Figures 5.4-5.5 show the influence of the staggered configuration on the blade loading. Increasing the span also increases the relative difference. Therefore, the

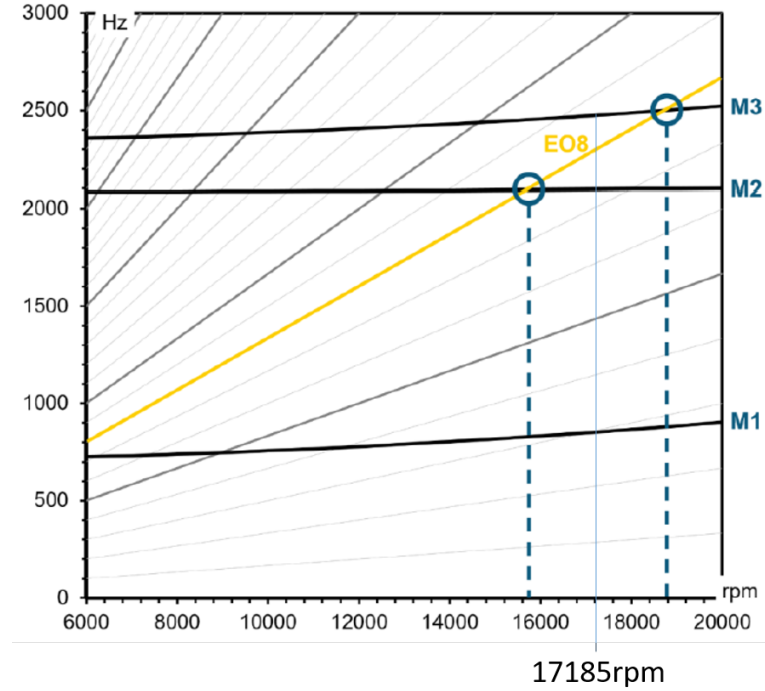


Figure 5.2: Campbell Diagram TUD compressor [14]

Inlet Total Pressure [Pa]	Outlet Static Pressure [Pa]	Outlet Total Pressure [Pa]	Pressure Ratio	Mass Flow Rate [kg/s]
101320	98000	119570	1.180	14.54
101320	102000	122177	1.206	14.54
101320	110000	128131	1.265	14.05
101320	113000	130151	1.285	13.86
101320	114000	130821	1.291	13.78
101320	115000	131489	1.298	13.71
101320	117000	132814	1.311	13.54
101320	120000	134791	1.330	13.26
101320	122500	136423	1.346	13.00

Table 5.1: Results of the iterative procedure

differences in the two patterns are high approaching the shroud: higher span sections are more loaded than the hub section. Generally speaking, the blade loading has a peak at the leading edge due to the frontal impingement of the fluid flow, while the pressure at the pressure side downstream is almost constant. The normal shock causes a rapid increase of the pressure and in this case it happens at

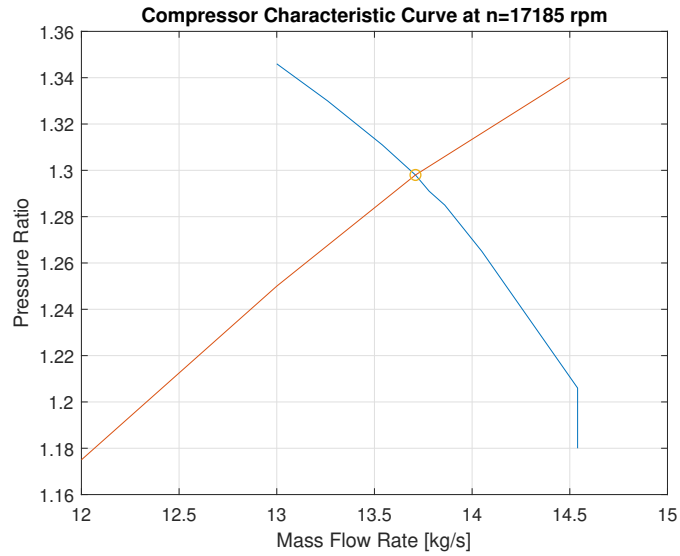


Figure 5.3: Compressor characteristic curve at $n=17,185$ rpm. The red circle marks the operating point in the staggered configuration. The red line approximately indicates the working line in the TUD pre-tests performance map

around 25% of the chord. The staggered configuration influences the Mach number and total pressure distribution as well.

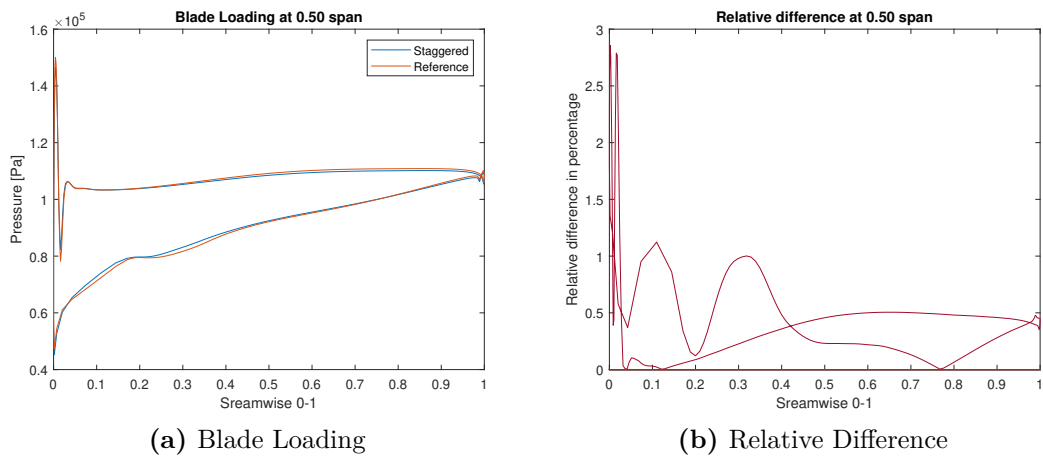


Figure 5.4: Blade Loading and Relative Difference, 50% span

From Figure 5.6, it is clear that the wake region is larger for the staggered blade, while the Mach distribution in OGV, stator and rotor is not affected much. At 95% span (5.7), there is a sensitive difference in the Mach number distribution at the

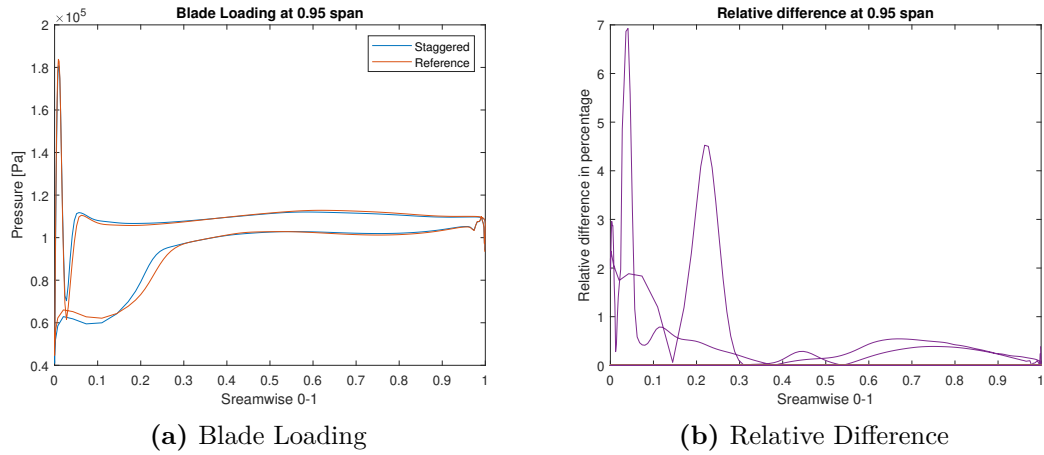


Figure 5.5: Blade Loading and Relative Difference, 95% span

stator pressure side. Regarding the rotor, at 50% span there is little difference in the Mach number distribution, while at 95% span there are more differences in the shock regions. It is interesting to notice that one can verify the correctness of the Mach number distribution with the blade loading. The supersonic Mach number at the inlet increases suddenly at the leading edge due to a bow shock: after that the fluid starts decelerating experiencing a shock at around 25% chord, causing an increase in pressure as a consequence. Besides, the pressure side is not influenced by the shock. The maximum Mach number is around 1.5.

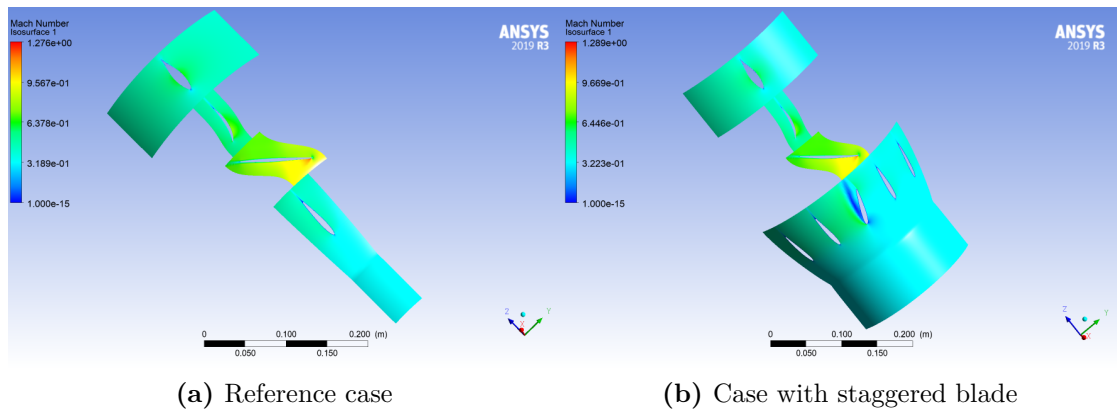


Figure 5.6: Mach number, 50% span

Regarding the total pressure distribution (Figures 5.8-5.9), the IGV with staggered blade has higher pressure losses, and this is likely to influence the blade

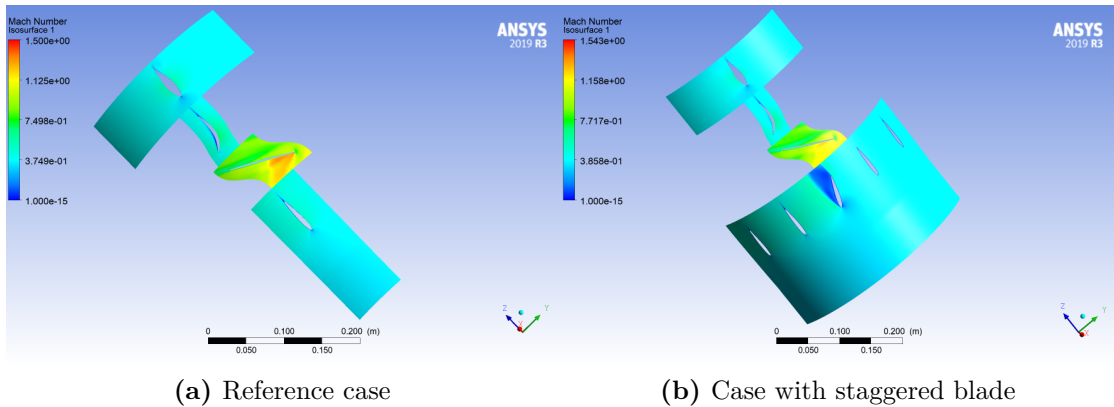


Figure 5.7: Mach number, 95% span

loading as well. At the rotor pressure side a wider total pressure loss is present: from Figures 5.6 and 5.7 it can be seen that this decrease of pressure is associated with a decrease in the Mach number, as expected. As a consequence, one can forecast that the static pressure is likely to increase more on the pressure side than on the suction side. Moreover, wakes at the trailing edge show losses and local decrease of the Mach number. These losses have to be carefully monitored and controlled since they could compromise efficiency and performance.

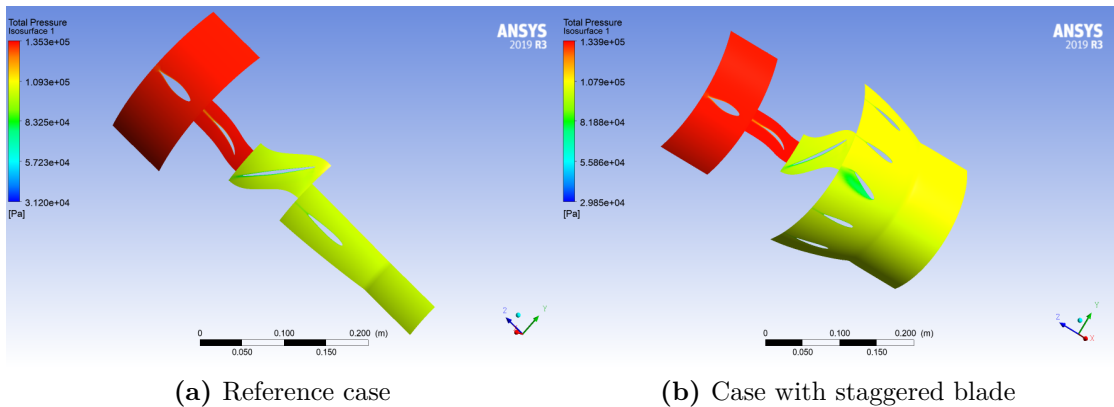


Figure 5.8: Total pressure, 50% span

It is important to notice that the operating points of the pattern A and C are close but not exactly the same, and this might affect the comparison. However, the maximum and minimum values of the shown variables are very close. Last but not least, shocks can be visualized by plotting the density gradient, as in Figure 5.10. The red areas indicate a high density gradient: as expected, these areas

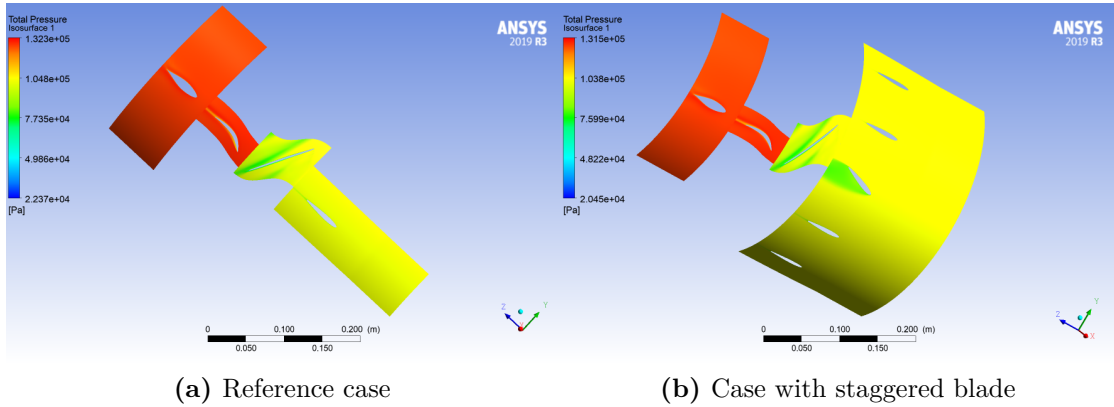


Figure 5.9: Total pressure, 95% span

correspond to the leading edges of the blades, and to the boundary layer regions. Regarding the wake generator, bow shocks can be observed in each leading edge. The shock with high intensity is the one at the staggered blade leading edge. Flow separation is also visible for the staggered blade. The density gradient plot for the rotor confirms the presence of a bow shock at the leading edge, and of a normal shock at around 25% chord on the suction side.

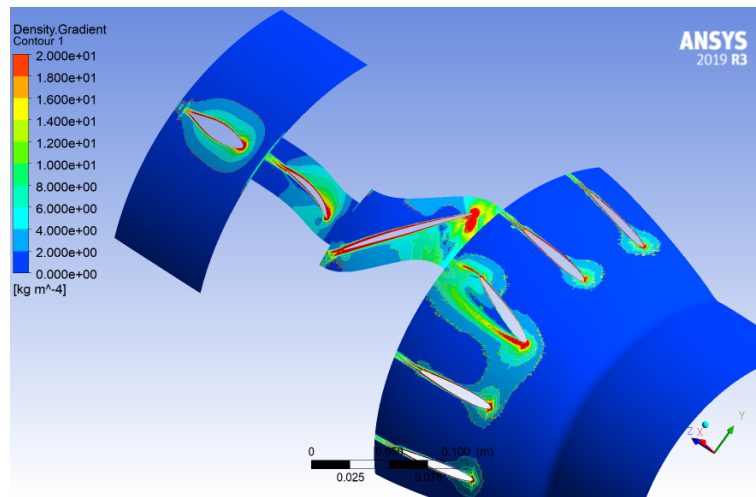


Figure 5.10: Density gradient plot on isosurface at 50% span. Shock regions can be clearly identified.

5.2 Steady State Simulations - Pattern B and C

In order to understand the influence of the staggered configuration, two unsteady simulations are run with the Time Transformation Method in CFX. Patterns B and C are taken into consideration (Figure 1.2). The reason behind this choice is related to the low computation time and memory required. In fact, if the second mode excited by engine order 15 (M2 EO15) is selected, just one rotor blade and one IGV has to be modeled, as shown in Figure 5.11.

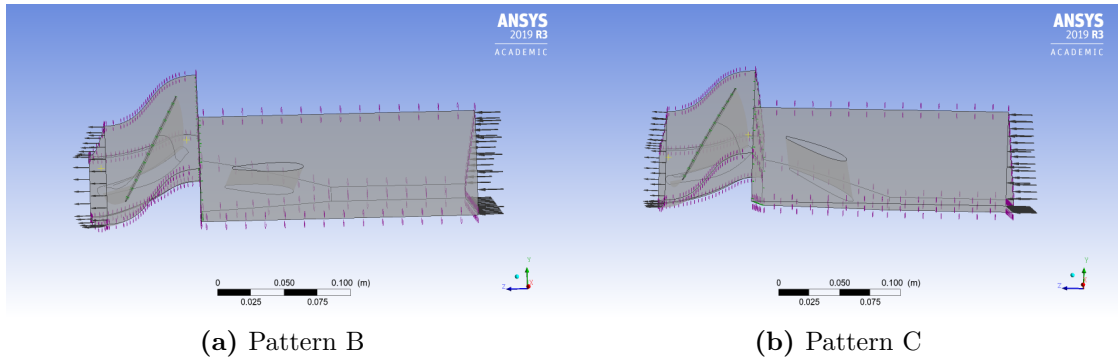


Figure 5.11: Total pressure, 95% span

However, a separate SS analysis has to be executed in each case before running the transient. First of all, looking at the Campbell diagram in Figure 5.2, the rotational speed of interest is around 8,681 rpm (intersection between M2 and the EO15 line), corresponding to a rotor blade frequency of 2,170.25 Hz. All the SS simulations has to be run at this speed.

Before running the transient analysis, it is important to reach a good convergence on the steady state solutions ($r = 10^{-6}$). The geometry for these simulations is the same as Figure 5.1, with the only difference that in the staggered blade setup all the straight blades are deleted (so 15 staggered blades can be reproduced). The operating point should be close to the TUD compressor design line, therefore an iterative procedure is applied, similar to the one performed for pattern A. The results of the iterations are shown in Table 5.2

After convergence, the rotor outlet SS conditions are exported to two new CFX files with geometry as in Figure 5.11. A steady state simulation is run for each pattern: the results of this simulation can be then used as initial value for the transient analysis and some interesting variables can be compared to check the accuracy of the transient simulations. For instance, one can calculate the aerodynamic force acting on the blade at the end of the simulation. This is realized by computing the area integral of the static pressure on the rotor blade.

	Inlet Total Pressure [Pa]	Outlet Static Pressure [Pa]	Outlet Total Pressure [Pa]	Pressure Ratio	Mass Flow Rate [kg/s]
Pattern B	101320	105000	109051	1.076	6.73
Pattern C	101320	105000	108175	1.068	5.99

Table 5.2: Operating points for pattern B and C at the new rotational speed (8,681 rpm)

In CFX-Post:

$$F = \text{areaInt}(\text{Pressure})@R1\text{Blade}$$

The result is $F_B = 1,518.4 \text{ N}$ for the pattern without staggered blades and $F_C = 1,514.7 \text{ N}$ for the one with just staggered blades. As expected, these values are very close to each other. Another parameter of interest is the torque. This variable has been monitored with CFX to further check the convergence. As shown in Figure 5.12, a good convergence for the torque value is reached: the value indicated in those plots is the torque calculated with respect to the y-axis, and it has the highest intensity compared to the x- and z- torque values.

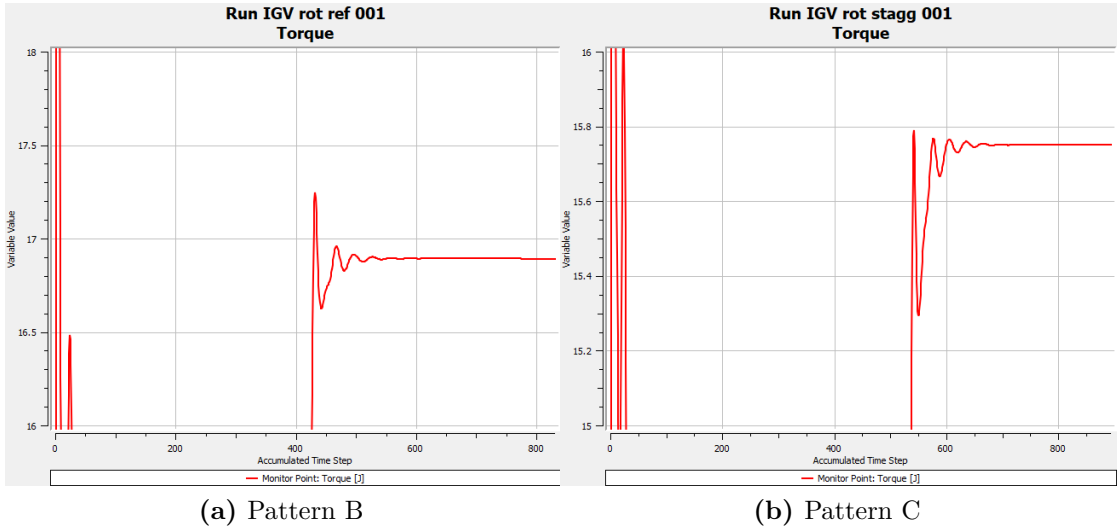


Figure 5.12: Convergence plot relative to the monitor of the torque with respect to the y-axis

The torque T with respect to the z-axis is a significant parameter to look at. It is calculated as the product between the blade loading or the pressure of the force impinging the blade and the distance from the shaft. Its value is $T_B = -3.22 \text{ N m}$

for pattern B and $T_C = -2.54 \text{ N m}$ for pattern C. The torque is correctly a negative value for the right-hand rule: the force is towards the negative y-axis, the distance is pointing at the negative x-axis, so the torque is directed towards the negative z-axis.

5.3 Unsteady Simulations - Patterns B and C

For the Time Transformation simulations, the condition of having pitch ratio close to unity is respected by modeling 2 blade passages in total. The following considerations are valid for both pattern B and C:

- IGV: 1 blade modeled, 15 blades in total. Applying equation 2.14, the passing period is $4.608 \times 10^{-4} \text{ s}$
- Rotor: 1 blade modeled, 16 blades in total. Passing period $4.320 \times 10^{-4} \text{ s}$

At the IGV-rotor and rotor-stator interface, *Transient Stator Rotor* is chosen as mixing model. The number of timesteps per period, as well as the number of coefficient loops, is chosen by running several simulation and finding a compromise between acceptable accuracy and computation time. For the two transient simulations, a number of time steps per period equal to 40 has been selected, with maximum 5 coefficient loops per iteration. The simulation is ended when a good convergence is reached regarding the residuals, and when the pressure oscillations become stable, with a minor difference in consecutive peaks (around 1%). The pressure is measured in two monitor points upstream and downstream the rotor blade.

Taking into account pattern B, the simulation is ended after 456 iterations, i.e. 11.4 pitches, when an almost periodic pattern is observed regarding the inlet total pressure. The residuals for momentum and mass and the inlet total pressure trend is shown in Figure 5.13. To notice that the RMS are monitored displaying all the iterations (also the ones of the previous steady state simulations). As regards pattern C, the simulation is ended 531 iterations, i.e. 13.275 pitches.

Some more iterations are needed for a more accurate solution in both cases, but some conclusions can be already drawn from the output files.

5.3.1 Results

At the last time step, some interesting conclusions can be drawn from the pressure and velocity plots. From the velocity plots (Figure 5.14), the shock at the rotor leading edge causes a sudden decrease in velocity. The shock at the suction side is also visualized, as in the steady state case. To notice that the last time step is used

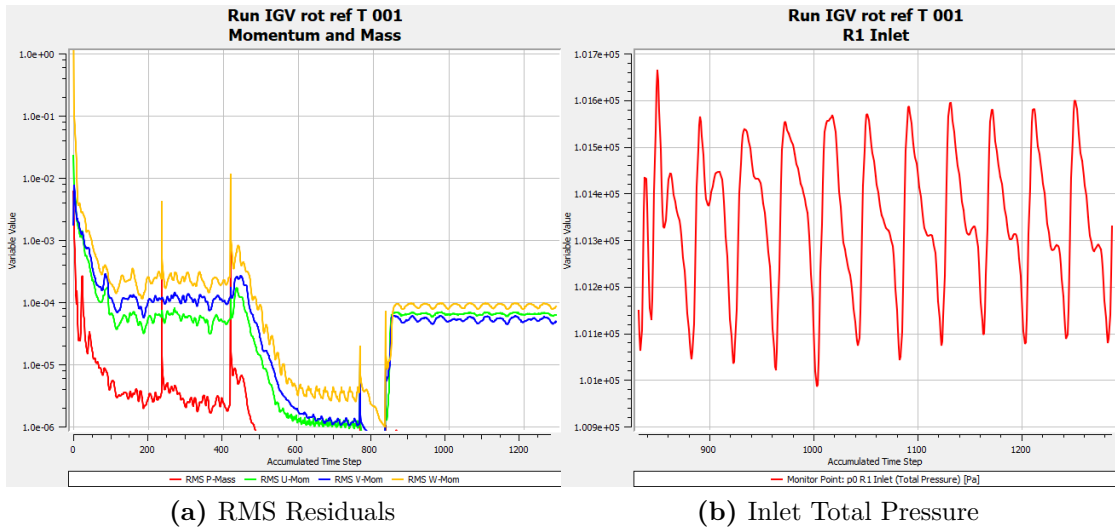


Figure 5.13: Residuals and inlet total pressure at the end of the simulation - Pattern B

for the plots, corresponding to a different phase for the patterns. For this reason the blade passage might look a bit different. Using a similar phase for the plots does not affect significantly the considerations previously done.

As a consequence of the shock, static pressure increases remarkably, and pattern B registers a higher maximum static pressure, close to the leading edge (around 112 kPa versus 109 kPa for pattern C).

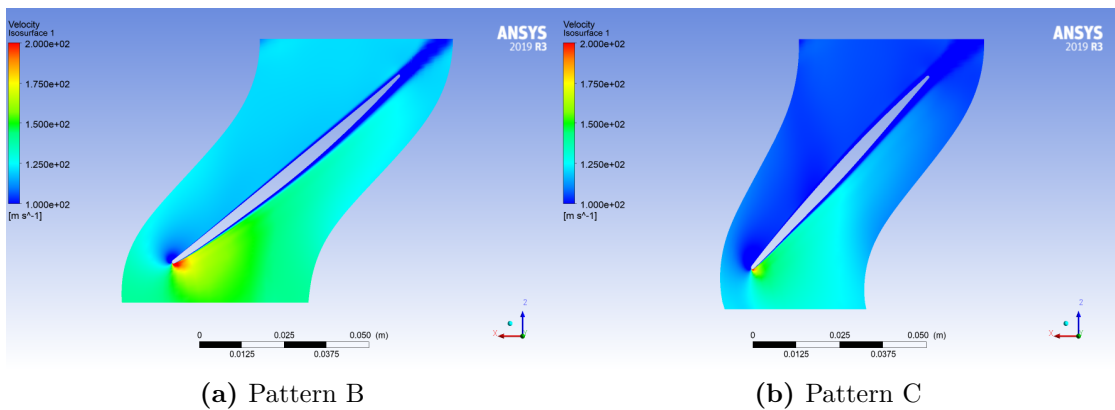


Figure 5.14: Velocity contour plot at 50% span, range 100 m/s-200 m/s

In order to understand better the effect of the staggered configuration on the aerodynamic forcing, the aerodynamic force can be calculated for each Fourier

coefficient for both pattern B and C. Its modulus can be computed implementing the following formula in CFX-Post.

$$F_{excitation} = \int_A \sqrt{p_{i,real}^2 + p_{i,imm}^2} dA \quad (5.1)$$

where i indicates the Fourier coefficient and p is the absolute pressure (real and imaginary part). First of all, for $i = 0$, one should obtain the same results as the steady state simulation (B=pattern B, C=pattern C):

$$F_B = 1,518.5 \text{ N} \qquad F_C = 1,514.7 \text{ N}$$

that is consistent with the steady state.

The Fourier spectrum can be plotted considering the first seven Fourier coefficients. Having 15 blades, the Fourier coefficient 1 corresponds to EO15, coefficient 2 to EO30, and so on until coefficient 7 (EO105). The aerodynamic force is associated at each Fourier coefficient. From the bar graphs in Figure 5.15, the first two coefficients are the most critical: those ones are corresponding to EO15 and EO30, scope of the thesis project. The staggered configuration generates higher forces in this case. Regarding the other coefficients, their value gets lower and lower as expected. Starting from EO60, the aerodynamic forces are slightly higher for the reference configuration compared to the staggered one. It is important to remark that being smaller, these results are more influenced by the incomplete convergence of the results.

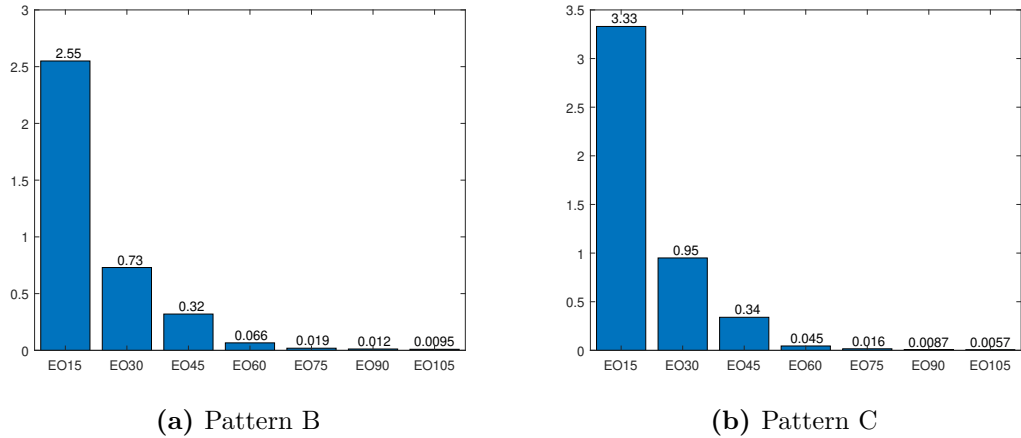


Figure 5.15: Fourier spectrum: the aerodynamic force contribution is plotted on the y-axis in Newton. On the x-axis, the Fourier coefficient corresponding to the engine orders are shown

Let us now analyze the locations at which the aerodynamic force critical. Only Fourier coefficients 1 and 2 are taken into account. These two are critical not

only for the high values of the aerodynamic contributions, but also because a superposition with the mode excitation may be possible. In fact, at that rotational speed, there are two intersections on the Campbell diagram: one is between the lines of EO15 and the second mode (already discussed), and the other one is given by the fifth mode line intersecting the EO30 curve, corresponding to a blade frequency of 4,340.5 Hz. The contour plots can then be investigated.

Regarding M2 EO15, the highest displacement is located at the blade tip for this mode shape. Let us check the absolute pressure distribution on the blade. From Figure 5.16, the staggered configuration is certainly more critical. The pressure is maximum at the leading edge, and more on the root than on the tip. The root is less risky than the tip regarding vibrations. However, at the tip of the suction side the pressure is quite high at the leading edge corner. For the reference pattern, no warning are given, also because the maximum values of pressure are located in a quite small region at the leading edge and they are smaller than the ones in pattern C. The overall pressure distribution (on both sides of the blade) is less critical as well, with quite high pressure values at the root on the pressure side, but smaller than the ones in pattern C.

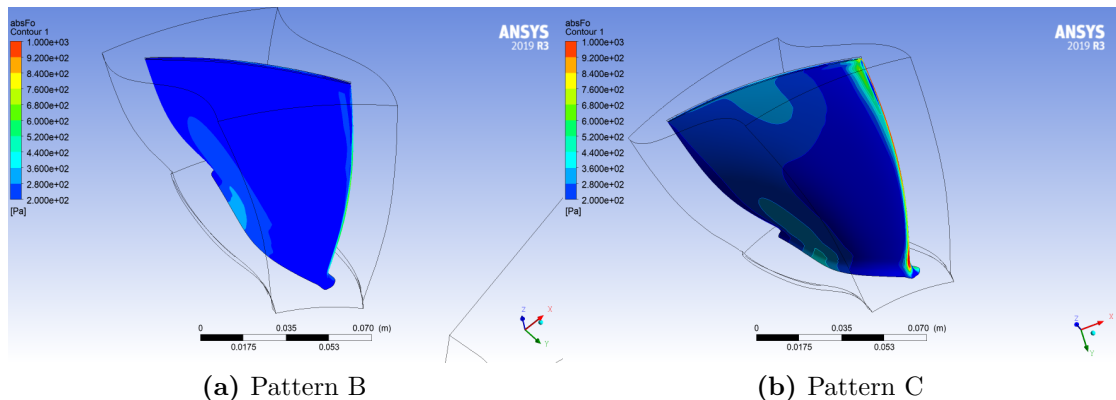


Figure 5.16: Absolute pressure contours at the rotor suction side - EO15. Range: 200 Pa-1,000 Pa

Regarding M5 EO30, the corresponding mode shape shows the highest deformation values at the blade tip and in two areas located towards the shroud at the leading and trailing edge of the blade¹. Let us check the absolute pressure distribution on the blade. From Figure 5.17, also in this case the staggered configuration generates more criticalities: the unsteady forces are again higher in areas of the

¹The shapes are obtained with ANSYS MECHANICAL for both pattern B and C, but not included in this thesis report

blade where there is a dangerous situation regarding structural vibrations. The pressure is maximum at the leading edge, and towards the tip, which is concerning. Even on the pressure side pressure is not negligible, in particular at mid-chord. Regarding the reference pattern, no warning are given, also because the maximum values of pressure are located in a quite small region at the leading edge at mid-span and they are smaller than the ones in pattern C. The overall pressure distribution (on both sides of the blade) is less critical as well, with quite high pressure values on both pressure and suction side in the first 10% of the chord, but smaller than the ones in pattern C.

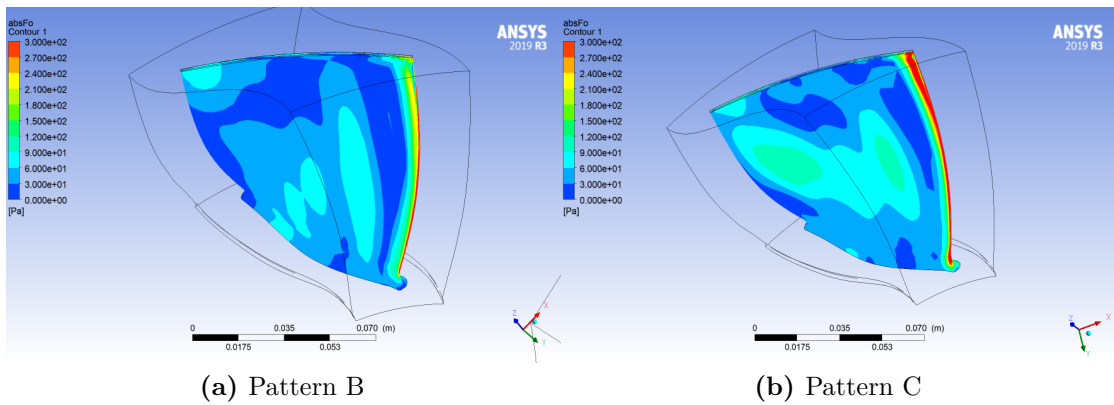


Figure 5.17: Absolute pressure contours at the rotor suction side - EO30. Range: 0 Pa-300 Pa

Chapter 6

Conclusions and Future Work

The results obtained in this thesis work will expand the ARIAS database, and will be useful for further investigations. In the next months, some more simulations will be carried out to obtain the forced response for the three patterns. This means that the path through which this research has been conducted is still long and the final destination has not been reached yet.

Regarding pattern A, the transient simulation with the Time Transformation Method can be run: after observing periodic oscillatory patterns of the rotor inlet pressure, the Fourier decomposition can be analyzed. The real and imaginary pressure can be extracted as done for pattern B and C. Because M1 EO3 is taken into account, one can compare the pressure trend on the blade with the reference case: just 3 IGV blades are needed to get an excitation of order 3. Therefore, some mesh adjustments will be needed.

To run a complete forced response, the modal analysis has to be computed for the blade using ANSYS Mechanical. Thanks to the FE blade discretization, the modes of interest can be obtained: for each mode, different nodal diameters can be considered. The final aim is to verify the simulation results with the experiments, i.e. amplitude as a function of the frequency and alternating and mean stress components (Haigh diagram). The mean stress component corresponds to the equivalent stress, which is an output of Static Structural analysis. The alternating stress and the amplitude are obtained with the Harmonic Response study. Before proceeding, the aerodynamic damping has to be calculated: this will allow to verify the patterns against flutter. A transient analysis using Fourier Transformation method has therefore to be performed. One of the outputs of this simulation is the wall work density which can be used to calculate the aerodynamic work. Applying the energy method, a damping factor can be computed and used in the Harmonic

Response settings. It is important to notice that this number strongly depends on the nodal diameters and on the direction of the traveling wave (backward or forward): a critical nodal diameter has to be found and used as input for determining the aerodamping. After obtaining the aerodynamic damping coefficient, all the variables needed for the Harmonic Response will have been computed. The output of this package will be the trend of the vibration amplitude as a function of the frequency (in a range around the critical frequency).

Further future considerations might be related to the introduction of mistuning in the patterns, with the final aim of reducing unwanted vibrations.

Appendix A

Theoretical Background

In this appendix, some further theoretical concepts are presented in addition to what has been already discussed in Chapter 2. In the first two sections, transonic flows and structural dynamics in turbomachinery is presented. In the third part, forced response is briefly discussed, and some CFD equations and principles are introduced in the last section.

A.1 Transonic Flow in Axial Compressors

The interest in transonic compressors has grown recently in the designers of aircraft engines. In this section, a qualitative analysis of transonic flows is performed: the reader can refer to more specialized literature for further information.

The reason why transonic flows are more studied is related to the higher pressure ratios, mass ratios and velocity that can be reached. Moreover, the compressor can be lighter, thus reducing the overall machine weight. These advantages are obtained thanks to the shock wave formation around the rotor blades. However, equations governing transonic phenomena cannot be linearized, and therefore the flow study is more difficult and challenging [7].

Transonic flows usually occur at Mach number between 0.8 and 1.2. In this range, compressibility cannot be neglected and the gas density varies locally during compression. In certain regions (i.e. rotor leading edge), shock waves can generate and lead to an almost instantaneous increase in static pressure, temperature and gas density. This process does not produce work, there is no heat addition and so total enthalpy and total temperature are constant. However, shocks are non-isentropic and irreversible, so the total pressure decreases from upstream to downstream (total pressure loss): Bernoulli's equation cannot be applied under this conditions. Flow velocity decreases after the shock and becomes lower than the sound velocity if the shock is normal, i.e. shock wave is perpendicular to the flow direction.

A careful analysis of what happens in a transonic blade passage is needed: shock waves, flow separation (downstream a normal shock due to strong flow deceleration) and secondary flows may occur. Those are source of instabilities (strong vibrations) and losses (for example in the total pressure). When $Ma > 0.4$, the fluid is decelerated and the pressure ratio increases with the Mach number. At a certain point, in some local regions of the stage, the sound speed can be attained and shocks may generate at rotor leading edge. The Mach number at which shocks originate is usually defined critical Mach number M_{cr} . Flow patterns showing different cases are depicted in Figure A.1.

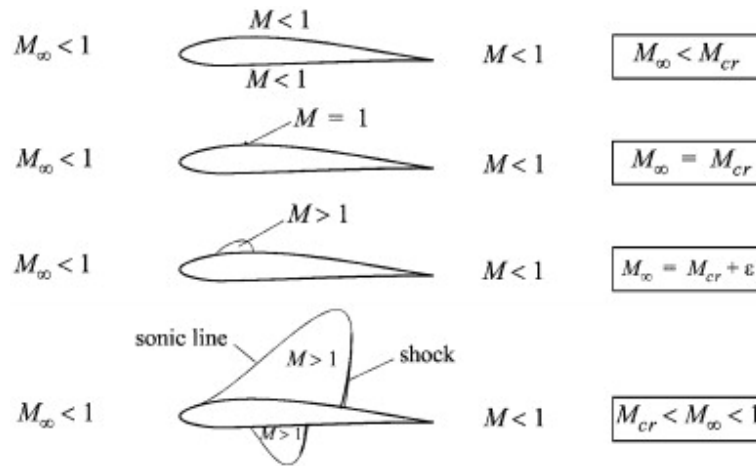


Figure A.1: Flow patterns in subsonic and transonic flows without boundary layer separation [7]

The leading edge shocks can extend upstream the blade generating noise and instability. In order to better regulate the flow at the rotor inlet, an IGV can be installed at the entrance. These stator blades allow to decrease of the relative inlet Mach number at the rotor entrance and thus the loading on the rotor blades [15]. Regarding supersonic flows, boundary layer separation occurs, reducing the pressure ratio and increasing losses. The normal shock that generates at the rotor leading edge can be attached or detached. Shocks generate at a certain vibration frequency, which depends on the flow velocity and on the boundary layer thickness. In case the oscillation induced by the shock is equal to the natural frequency of the rotor blade, some dangerous instabilities may be produced, such as the supersonic unstalled flutter.

A.2 Structural Dynamics in Turbomachinery

Let us recall the general concepts to understand the characteristics of a vibrating structure. Considering the mass-spring-damper model, the equation of motion can be written as:

$$m\ddot{x} + c\dot{x} + kx = F(t) \quad (\text{A.1})$$

where the simple case of one DOF is considered: in equation A.1, m indicates the mass, c the viscous damping coefficient and k the stiffness. It can be shown that in case of MDOF, the equation can be still written in that form, but the variable x has to be replaced by a vector \mathbf{x} containing the displacement in all the directions where motion is possible and mass, damping and stiffness are replaced by matrices. The force $F(t)$ is time-dependent and it is set to zero in case of free vibrations (natural), while it is different from zero in case of forced vibrations (when a force causes the structure to vibrate) [16]. The two cases are analyzed below.

A.2.1 Free Vibrations

Assuming $F(t)$ equal to 0 in equation A.1, and considering the general solution to the free damped equation, it follows [17]:

$$\begin{aligned} x &= Ce^{rt} \\ \left(r^2 + \frac{c}{m}r + \frac{k}{m} \right) e^{rt} &= 0 \\ r_{1,2} &= -\frac{c}{2m} \pm \sqrt{\frac{c^2}{4m^2} - \frac{k}{m}} \\ x &= e^{\frac{-ct}{2m}} \left(C_1 e^{\sqrt{\frac{c^2}{4m^2} - \frac{k}{m}}t} + C_2 e^{\sqrt{\frac{c^2}{4m^2} - \frac{k}{m}}t} \right) \end{aligned}$$

The value of damping ratio that makes the square root at the exponential equal is called critical damping ratio and by definition:

$$c_{crit} = 2m\omega = \sqrt{4mk} \quad (\text{A.2})$$

The damping factor can be defined as:

$$\zeta = \frac{c}{c_{crit}} \quad (\text{A.3})$$

In Figure A.2 the influence of the damping factor on the overall system behaviour can be analyzed. This is of primary importance in the design of aerospace components. Based on the values of ζ , the system can be defined as:

- Critically damped if $\zeta = 1$
- Over-damped if $\zeta > 1$
- Under-damped if $\zeta < 1$

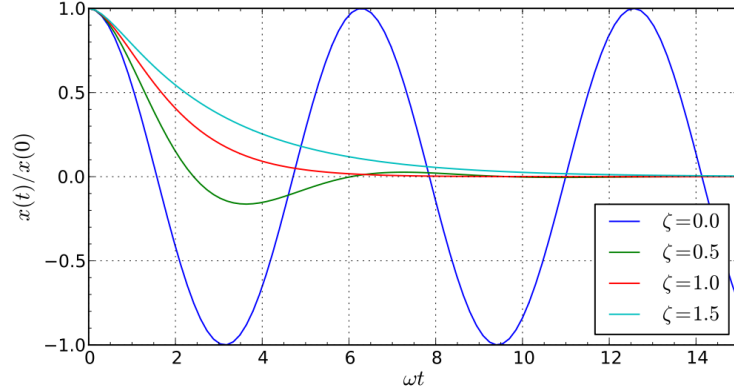


Figure A.2: Normalized coordinate as a function of different values of ζ

A.2.2 Forced Vibrations

Let us focus on the particular case in which the forcing term in Equation A.1 is harmonic

$$F(t) = F_0 \sin \omega t$$

The SS solution for this problem can be written as:

$$x = X_0 \sin \omega t + \phi$$

which means that the system will oscillate at the same frequency $f = \omega/(2\pi)$ but with a certain phase difference ϕ with respect to the forcing term. By substituting into the equation of motion, two expressions can be obtained, one for the amplitude of the vibration X_0 and one for the phase. Both expressions are function of ζ and $r = \frac{\omega}{\omega_n}$ (frequency ratio).

$$X_0 = \frac{F_0}{k} \frac{1}{\sqrt{(1-r^2)^2 + (2\zeta r)^2}} \quad (\text{A.4})$$

$$\phi = \arctan \frac{-2\zeta r}{1-r^2} \quad (\text{A.5})$$

By plotting Equations A.4 and A.5, the so-called "frequency-response of the system" can be summarized (Figure A.3). To notice that if $r \approx 1$ and if damping is low, the vibrations can become very high and they can lead to severe damage of the engines. This point is called *resonance point*. As it is shown in the next section, in the case of MDOF there are more than one resonance point and one of the aims of the vibration analysis is to predict when these resonances may occur and then to determine how to prevent it from occurring. As the amplitude plot shows, adding damping can significantly reduce the magnitude of the vibration. Also, the magnitude can be reduced if the natural frequency can be shifted away from the forcing frequency by changing the stiffness or mass of the system.

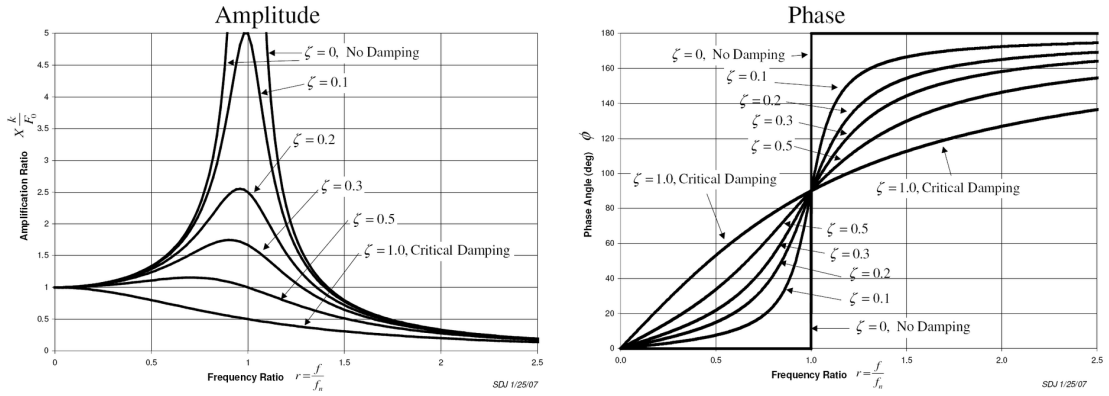


Figure A.3: Frequency response plots: amplitude (*left*) and phase (*right*)

A.2.3 MDOF Systems

In case more than one DOF is taken into account, Equation A.1 becomes:

$$[M]\ddot{\mathbf{x}} + [C]\dot{\mathbf{x}} + [K]\mathbf{x} = \mathbf{f} \quad (\text{A.6})$$

where $[M]$, $[C]$ and $[K]$ are matrices $n \times n$ (n is the number of degrees of freedom) and \mathbf{x} is a vector $n \times 1$. Assuming no damping and no forcing term, and considering synchronous solution in the form

$$\mathbf{x} = \mathbf{x}_0 \cos \omega t + \phi$$

Equation A.6 can be written in the form of an Eigenvalue Problem:

$$([K] - \omega^2[M])\mathbf{x}_0 = 0 \quad (\text{A.7})$$

the non-trivial solutions can be found by solving the characteristic equation:

$$\det([K] - \omega^2[M]) = 0 \quad (\text{A.8})$$

The square roots of the eigenvalues are the natural frequencies of the system

$$0 \leq \omega_1 \leq \omega_2 \leq \dots \leq \omega_n \quad (\text{A.9})$$

and by substituting each eigenvalue ω_i^2 in Equation A.7 the eigenvectors Φ_i are obtained. The eigenvectors are the mode shapes of the natural modes, and they represent the susceptibility of a mode to a certain excitation. Moreover, it causes the vibratory stresses together with the vibration amplitude which influences the deformation.

Structural dynamics mainly deals with complex structure in which it is not always possible a simplification of the system, i.e. a discretization from a continuous system to a MDOF. At this point, 2 main turbomachinery components are analyzed: blades and disks. As a first remark, one should distinguish between flexible components that usually feature low natural frequencies (long and slim blades) and rigid components with high natural frequencies (short and strong blades). The first category is the main concern because they are more prone to have vibration problems and the current trends in manufacturing are going towards lean and slim blade design. When vibrations occur in a blade row, vibratory stresses generate and accumulate eventually leading to fatigue failure [18]. The maximum stress a blade can bear is a function of the material properties and of the ambient condition. As shown in Figure A.4, the tolerable vibratory stress is expressed as a mean stress σ_m , while the response amplitude characterizes the alternating stress component σ_a . The operating point can be consequently identified on the Haigh Diagram [19]. If outside the safe region, fatigue mechanisms may initiate and the crack propagation could occur. For this reason, it is really important to understand how both blades and disks behave when vibrations occurs to correctly estimate the operating point.

A.2.4 Structural Dynamics of Blades and Disks

In this section the structural dynamics of the most critical turbomachinery components (blades and disks) is taken into account, i.e. how these components can vibrate, both freely and in case of an external excitation.

Structural Dynamics of Blades

To simplify the analysis, blades can be regarded as *cantilevers*, i.e. thin beams clamped on one end. This approximation is more accurate for the compressor blades rather than the turbine ones, since usually turbine blades have usually higher

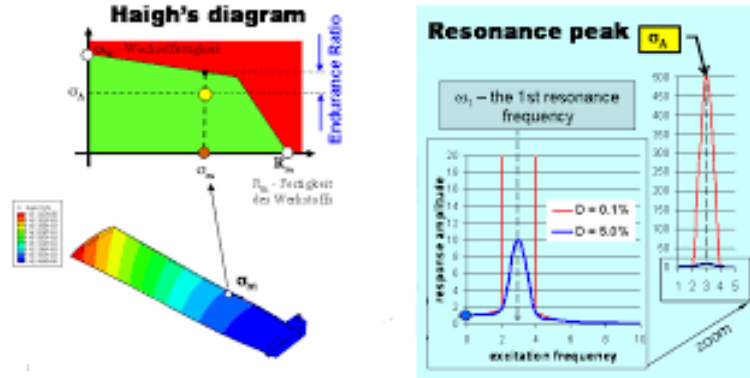


Figure A.4: a) Haigh Diagram. The green area is the "safe zone" (infinite life). R_m is the UTS (Ultimate Tensile Strength) and $\sigma_w = \sigma_e$ is the endurance limit. The first mode shape (bending) is represented. b) Frequency response amplitude for the SS excitation. D is the damping magnitude. [19]

curvature. A cantilever beam can experience 3 main modes: bending in x-direction, bending in y-direction and torsion. The frequency of oscillation can be written as:

$$\omega_n = a_n \sqrt{\frac{EI}{\mu_l l^4}} \quad (\text{A.10})$$

in which EI is the bending stiffness, μ_l is the mass per unit length and l is the length of the beam. The coefficient a_n vary as a function of the mode and they are shown in Table A.1. In this table, the mode shapes corresponding to the first 5 modes can be also seen.

The natural frequencies in case of torsional vibrations are expressed as:

$$\omega_n = n\pi \sqrt{\frac{GI_p}{\mu_l l^2}} \quad (\text{A.11})$$

where GI is the torsional stiffness and μ_l the moment of inertia per unit length.

The main three blade modes are shown in Figure A.5: first flap mode (bending normal to the skeleton line), second flap mode, and first torsion mode (torsion around the stacking line) [20]. In each mode configuration, one or more curves with zero curvature, where the the deflection changes sign can be identified, namely inflection lines.

Structural Dynamics of Disks

Disks can be simplified as circular flat plates, whose basic modes are:

- deflection in axial direction

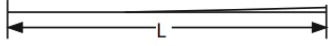
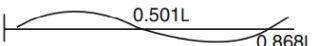
Mode Number (n)	a_n	Mode shape
1	3.52	
2	22.0	
3	61.7	
4	121.0	
5	200.0	

Table A.1: Natural frequencies and normal modes for cantilever beams.

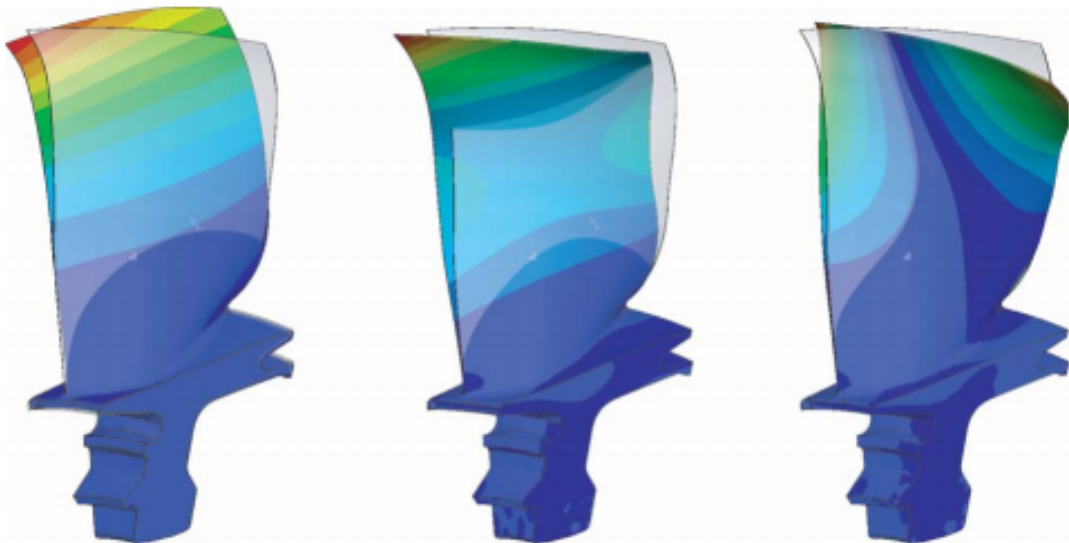


Figure A.5: Fundamental blade vibration modes: first flap mode (*left*), second flap mode (*middle*), first torsion mode (*right*) [20]

- deflection in radial direction
- deflection in tangential direction

The inflection lines are extended over the diameter length, for this reason they

are referred as ND (Nodal Diameter). In some more complex excitations, nodal circles can be defined as well. Figure A.6 depicts examples of mode shapes.

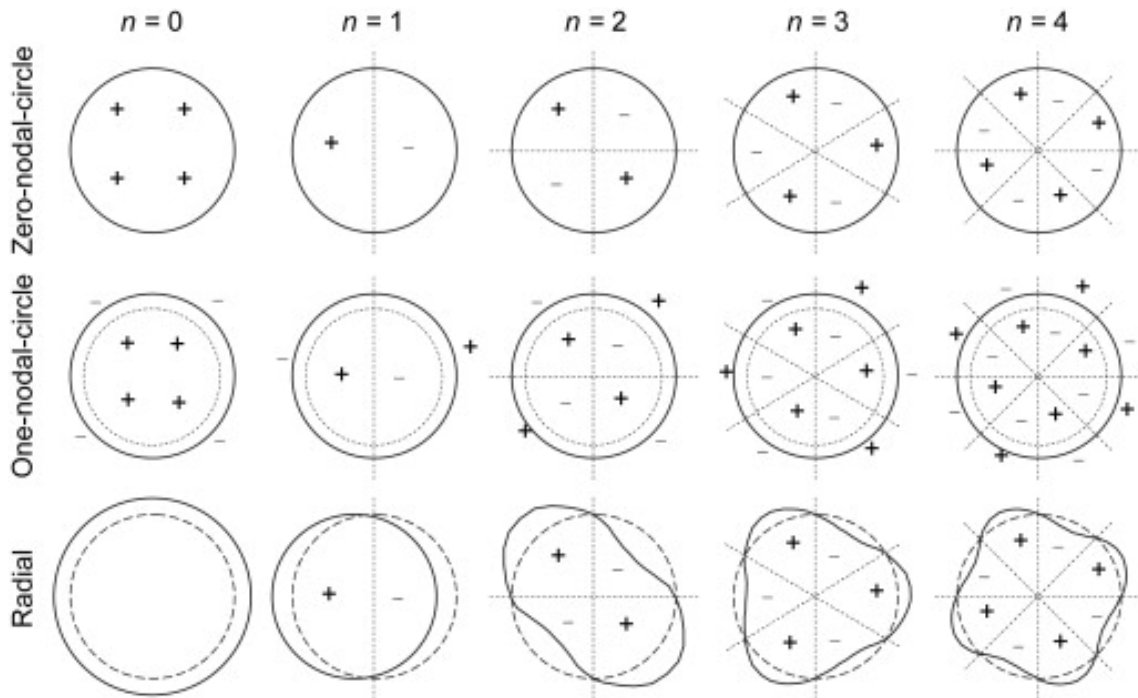


Figure A.6: Examples of mode shapes of a wheel, +/- indicates the relative phase of the motion in each area, —:deformed shape, - - -: undeformed shape, · · · · : node lines

Structural Dynamics of Bladed Disks

When considering blades and disks together, two different situations can occur:

- long blades and stiff disk: blade modes are dominant, i.e. the blade vibrates as it was set to ground
- stiff blades and flexible disk: disk modes are dominant

As shown in Figure A.7, *blade alone* modes do not depend on ND, while *disk alone* modes are varying as a function of the natural frequency, since the disk is coupled sector-to-sector. For low ND, the blade modes are disk-dominated, and the region where the 2 curves approach is called *veering*, which can lead to a change in natural frequency.

At this point, there is one last essential remark that has to be done: if the blades vibrate in a *tuned way*, i.e. in the same mode, at the same frequency and at the

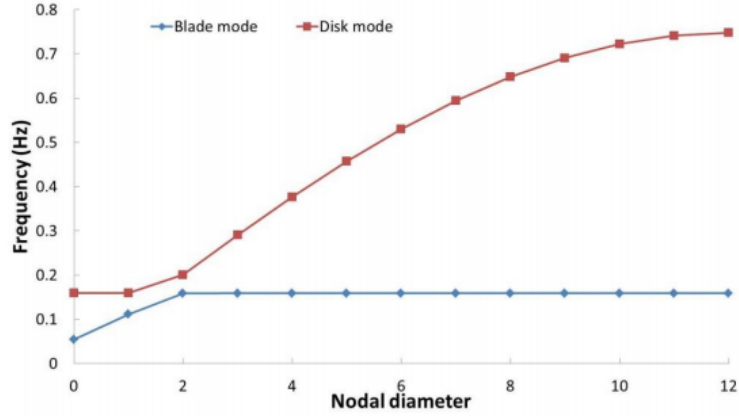


Figure A.7: Natural Frequency vs Nodal Diameter

same amplitude, a *traveling wave mode* is obtained. The *interblade phase angle* β characterizes the phase lag between two adjacent blades.

$$\text{Forward traveling wave: } \beta = \frac{2\pi ND}{N}$$

$$\text{Backward traveling wave: } \beta = \frac{2\pi(N - ND)}{N}$$

in which N is the number of blades and ND is the nodal diameter. Figure A.8 shows a configuration for $ND=1$ and $ND=3$.

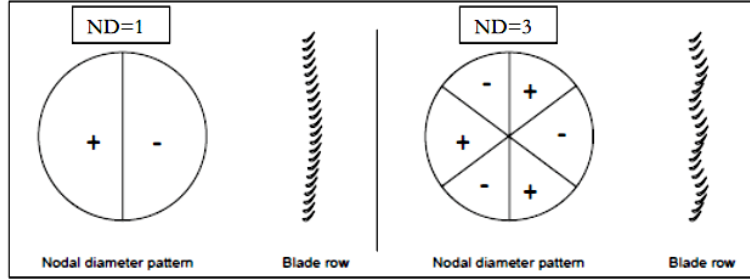


Figure A.8: Nodal diameter modes and wave modes for a blade row.

A.3 Forced Response

In this section, the forced response is mentioned for a matter of completeness. From the aeroelasticity equation 2.5, let us solve for the \mathbf{x} vector, once both \mathbf{F}_{coupl} and

\mathbf{F}_{exc} have been calculated. Equation 2.5, can be written as:

$$[-M_{str}\omega^2 + (C_{str} + C_{aero})\omega i + (K_{str} + K_{aero})]\mathbf{x} = \mathbf{F}_{EXC} \quad (\text{A.12})$$

where k_{aero} is very small and hence negligible. C_{aero} is the aerodynamic damping obtained through flutter analysis (not considered in this thesis work), which is bigger than C_{str} . \mathbf{x} is the physical coordinate giving information about vibrations (and therefore stresses). To reduce the computational time and simplify the equation, it is better to express Equation A.12 in generalized coordinates.

Let us define the matrix of modes \mathbf{V} , in which each column represents the eigenvectors associated to a specific mode. If the first three modes are considered, the matrix has dimension $n \times 3$. Recalling the MDOF theory [17]:

$$\begin{aligned} \mathbf{x} &= \mathbf{V}\mathbf{q} \\ [-\mathbf{V}^T M_{str} \mathbf{V} \omega^2 + \mathbf{V}^T (C_{str} + C_{aero}) \mathbf{V} \omega i + \mathbf{V}^T (K_{str} + K_{aero}) \mathbf{V}] \mathbf{q} &= \mathbf{V}^T \mathbf{F}_{exc} \\ [-\mathbf{I} \omega^2 + \mathbf{C}_q \omega i + \omega_n^2] \mathbf{q} &= \mathbf{V}^T \mathbf{F}_{exc} \end{aligned}$$

The equation to obtain the generalized coordinates is the following:

$$\mathbf{q} = [-\mathbf{I} \omega^2 + \mathbf{C}_q \omega i + \omega_n^2]^{-1} \cdot \mathbf{V}^T \mathbf{F}_{exc} \quad (\text{A.13})$$

where $\mathbf{V}^T \mathbf{F}_{exc}$ is the generalized force vector and represents the projection of the forcing function on each mode. The problem is therefore simplified into a system of single DOF equations. By computing Equation A.13, the trend of the vibration amplitude as a function of the frequency (related to ω) can be determined. A proper sweeping interval for the frequency can be set.

A.4 CFD

A.4.1 Governing Equations

The Navier-Stokes equations for compressible flows in the conservative form can be written using Einstein's notation in the following way [21]:

$$\begin{aligned} \text{Continuity Equation: } & \frac{\partial \rho}{\partial t} + \frac{\partial(\rho u_i)}{\partial x_i} \\ \text{Momentum Equation: } & \frac{\partial(\rho u_i)}{\partial t} + \frac{\partial(\rho u_i u_j)}{\partial x_j} = -\frac{\partial p}{\partial x_i} + \frac{\tau_{ij}}{\partial x_j} + S_M \\ \text{Energy Equation: } & \frac{\partial(\rho h_{tot})}{\partial t} - \frac{\partial p}{\partial t} + \frac{\partial(\rho u_j h_{tot})}{\partial x_j} = \frac{\partial}{\partial x_j} \left(\lambda \frac{\partial T}{\partial x_j} \right) + \frac{\partial(u_i \tau_{ij})}{\partial x_j} + S_E \end{aligned}$$

where S_M and S_E represent the source terms and in case of Newtonian fluids the stress tensor is related to the strain rate:

$$\tau_{ij} = \mu \left[\left(\frac{\partial u_i}{\partial x_j} + \frac{\partial u_j}{\partial x_i} \right) - \frac{2}{3} \delta_{ij} \frac{\partial u_k}{\partial x_k} \right] \quad (\text{A.14})$$

The RANS equations are obtained starting from the decomposition of the instantaneous velocity in the Navier-Stokes equations into a mean and a fluctuating component [21]. An extra term is obtained, called the Reynolds stress, which is modeled using a turbulence model. In this study, SST models are taken into account.

A.4.2 Turbulence Model

Let us now define the equations of the SST $k - \omega$ turbulence model, which is an extremely powerful model for adverse pressure gradients, but it requires high computational cost. The two equations of the model are the following:

$$\begin{aligned} \text{k-Equation: } & \frac{\partial(\rho k)}{\partial t} + \frac{\partial(\rho U_j k)}{\partial x_j} = \frac{\partial}{\partial x_j} \left[\left(\mu + \frac{\mu_t}{\sigma_{k1}} \right) \frac{\partial k}{\partial x_j} \right] + P_k - \beta^* \rho k \omega \\ \omega\text{-Equation: } & \frac{\partial(\rho \omega)}{\partial t} + \frac{\partial(\rho U_j \omega)}{\partial x_j} = \frac{\partial}{\partial x_j} \left[\left(\mu + \frac{\mu_t}{\sigma_{\omega 1}} \right) \frac{\partial \omega}{\partial x_j} \right] + \alpha_1 \frac{\omega}{k} P_k - \beta_1 * \rho \omega^2 \end{aligned}$$

The turbulent viscosity is defined as:

$$\nu_t = \frac{\mu_t}{\rho} = \frac{k}{\omega}$$

The term P_k contains information about the Reynolds stresses and the Boussinesq assumption is considered in order to compute its value. Turbulent viscosity is introduced to model the Reynolds stresses:

$$-\overline{u'_i u'_j} = \nu_t \left(\frac{\partial U_i}{\partial x_j} + \frac{\partial U_j}{\partial x_i} \right) - \frac{2}{3} \delta_{ij} \left(k + \nu_t \frac{\partial U_k}{\partial x_k} \right)$$

By means of the turbulence frequency, defined as $\omega = \varepsilon/k$, the $k - \varepsilon$ model can be transformed into $k - \omega$ model. In this new model, the equations can be written as

$$\begin{aligned}
 \text{k-Equation: } & \frac{\partial(\rho k)}{\partial t} + \frac{\partial(\rho U_j k)}{\partial x_j} = \frac{\partial}{\partial x_j} \left[\left(\mu + \frac{\mu_t}{\sigma_{k2}} \right) \frac{\partial k}{\partial x_j} \right] + P_k - \beta^* \rho k \omega \\
 \text{\omega-Equation: } & \frac{\partial(\rho \omega)}{\partial t} + \frac{\partial(\rho U_j \omega)}{\partial x_j} = \frac{\partial}{\partial x_j} \left[\left(\mu + \frac{\mu_t}{\sigma_{\omega 2}} \right) \right] \frac{\partial \omega}{\partial x_j} + \\
 & + 2\rho \frac{1}{\sigma_{\omega 2} \omega} \frac{\partial k}{\partial x_j} \frac{\partial \omega}{\partial x_j} + \alpha_2 \frac{\omega}{k} P_k - \beta_2 \rho \omega^2
 \end{aligned}$$

Neglecting the buoyancy term, the two equations in the SST $k - \omega$ model can be rewritten as:

$$\begin{aligned}
 \text{k-Equation: } & \frac{\partial(\rho k)}{\partial t} + \frac{\partial(\rho U_j k)}{\partial x_j} = \frac{\partial}{\partial x_j} \left[\left(\mu + \frac{\mu_t}{\sigma_{k3}} \right) \frac{\partial k}{\partial x_j} \right] + P_k - \beta^* \rho k \omega \\
 \text{\omega-Equation: } & \frac{\partial(\rho \omega)}{\partial t} + \frac{\partial(\rho U_j \omega)}{\partial x_j} = \frac{\partial}{\partial x_j} \left[\left(\mu + \frac{\mu_t}{\sigma_{\omega 3}} \right) \right] \frac{\partial \omega}{\partial x_j} + \\
 & + (1 - F_1) 2\rho \frac{1}{\sigma_{\omega 2} \omega} \frac{\partial k}{\partial x_j} \frac{\partial \omega}{\partial x_j} + \alpha_3 \frac{\omega}{k} P_k - \beta_3 \rho \omega^2
 \end{aligned}$$

where:

$$\begin{aligned}
 P_k &= \left(2\nu_t s_{ij} s_{ij} - \frac{2}{3} k \frac{\partial v_i}{\partial x_j} \delta_{ij} \right) \\
 F_1 &= \tanh \zeta^4 \\
 \text{with } \zeta &= \min \left[\max \left\{ \frac{\sqrt{k}}{\beta^* \omega y}, \frac{500\nu}{y^2 \omega} \frac{4\rho k}{CD_{k\omega} \sigma_{\omega 2} y^2} \right\} \right] \\
 \text{and } CD_{k\omega} &= \max \left\{ 2\rho \frac{1}{\sigma_{\omega 2} \omega} \frac{\partial k}{\partial x_j} \frac{\partial \omega}{\partial x_j}, 1 \cdot 10^{-10} \right\}
 \end{aligned}$$

The turbulent viscosity is defined as

$$\nu_t = \frac{a_1 k}{\max \left\{ a_1 \omega, SF_2 \right\}} \quad (\text{A.15})$$

in which:

$$\begin{aligned}
 SF_2 &= \tanh \eta^2 \\
 \text{with } \eta &= \max \left\{ \frac{2k^{1/2}}{\beta^* \omega y}, \frac{500\nu}{y^2 \omega} \right\}
 \end{aligned}$$

Near the wall, $F_1 = 1$, the model behaves as a $k - \omega$ model but far from the wall, $F_1 = 0$, the model behaves as a $k - \varepsilon$ model.

Appendix B

Additional Information to the Simulations

In this chapter one can find further information on the mesh generation with ICEM CFD. The main simulation settings are also presented for each simulation.

B.1 IGV Meshing with ICEM CFD

As a first step, the blade passage has to be modeled using ICEM *Geometry* function. Figures B.1 and B.2 the geometry for the non-staggered sector is shown. The inlet geometry is an annulus sector of angle 24° (symmetric with respect to the blade vertical axis). Regarding the outlet, in the preliminary phase an annulus sector is drawn as well, but this surface is modified when running simulations including the rotor. In fact, the rotor inflow surface is an irregular surface and has to be matched with the IGV outlet.

B.1.1 Blocking Strategy

The blocking strategy chosen for the hexa meshing is shown in Figure B.3. The blade does not have sharp leading or trailing edge angles, so the best way to mesh the geometry is to create an *O-grid* and use the function *Split blocks* to have more control over the regions before and after the blade. *Edit Associations* allows to associate the blocking surfaces to the geometry surfaces, so the mesh is projected on the corresponding faces (hub, shroud, interface, inlet, outlet, blade). Figures B.4a and B.4b represent the final result of the blocking procedure for the 2 most important faces (hub and shroud), since all the rest of the mesh depend on them. Details on the blade for the shroud and the hub are shown in Figures B.5b and B.5a. To obtain smoother mesh around the blade profile, the function *Split Edge*

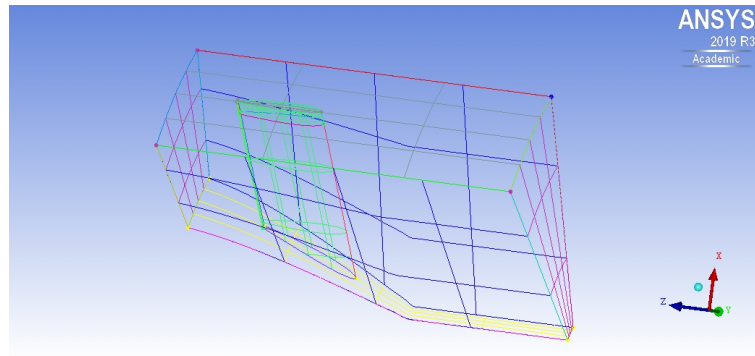


Figure B.1: Blade passage for the non-staggered configuration. Curves, surfaces and points are shown. *Yellow:* Hub. *Gray:* Shroud. *Blue:* Interface. *Green:* Blade. *Purple:* Inlet and Outlet

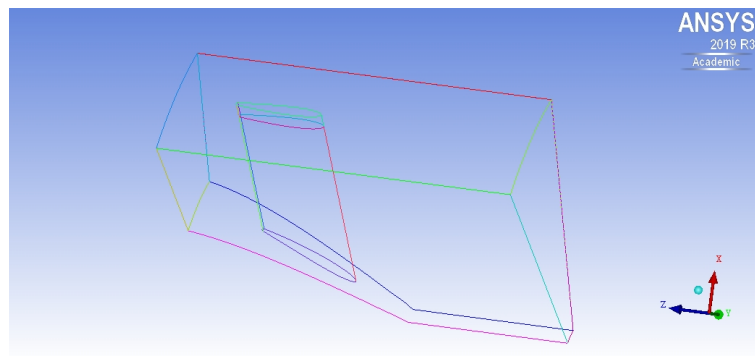


Figure B.2: Blade passage for the non-staggered configuration. Curves are shown

provides a wide variety of ways one can split the edge to better follow a certain curve. *Control Point* is chosen to split the edges at the shorter edges of the O-grid (trailing and leading edge), *Linear* is used on the blade curve (this helps avoiding negative volume regions as explained later), *Spline* on the longer edges of the O-grid, corresponding to the long edges of the blade profile.

Regarding the staggered blade, the blocking structure is obtained with a similar procedure (Figures B.6, B.7a-B.7b, B.8a-B.7b).

B.1.2 Pre-Mesh

After the blocking structure is set, the pre-meshing parameters have to be adjusted to guarantee an appropriate mesh resolution, especially in the boundary layer regions. The spacing of the mesh along the edge is determined by controlling several parameters, such as number of nodes, the meshing law, initial length at the

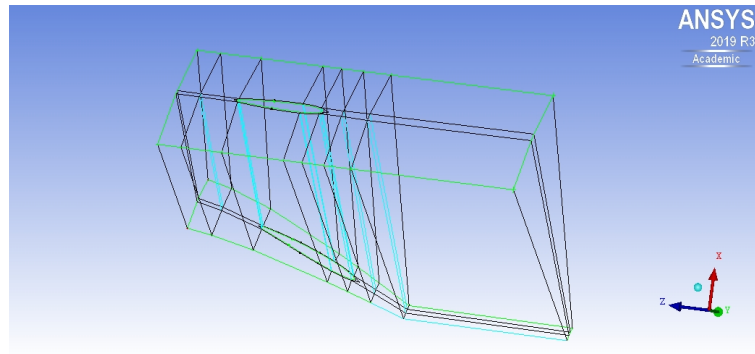
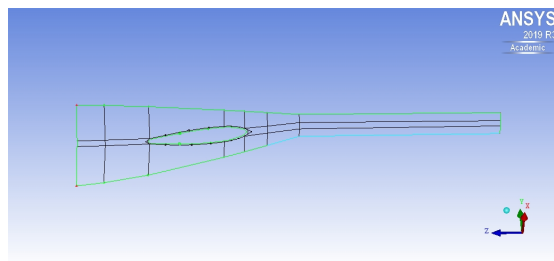
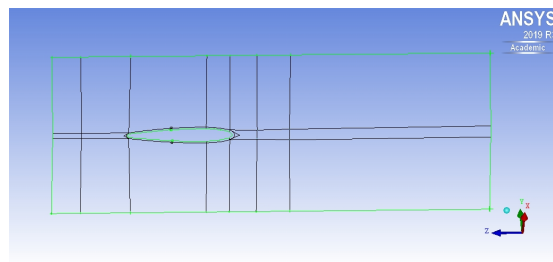


Figure B.3: Blocking of the reference blade sector



(a) Hub blocking topology



(b) Shroud blocking topology

Figure B.4: Block topology details: hub and shroud

beginning/end of the edge, the expansion of the mesh from the beginning/end of the edge to the interior, and the maximum element length along the edge.

For this reason, a minutious procedure is applied, following these steps, not to be performed necessarily in order:

- Edge selection and number of nodes definition.
- Choice of the mesh laws (or bunching laws). The most used ones are *BiGeometric* and *Hyperbolic*. The former is the default bunching law, based on parabolic spacing. The parabolas are defined starting from the two initial

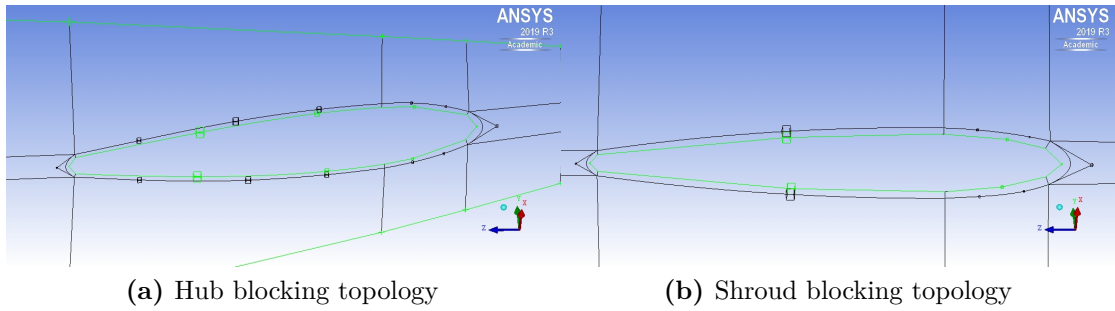


Figure B.5: Block topology details: hub and shroud

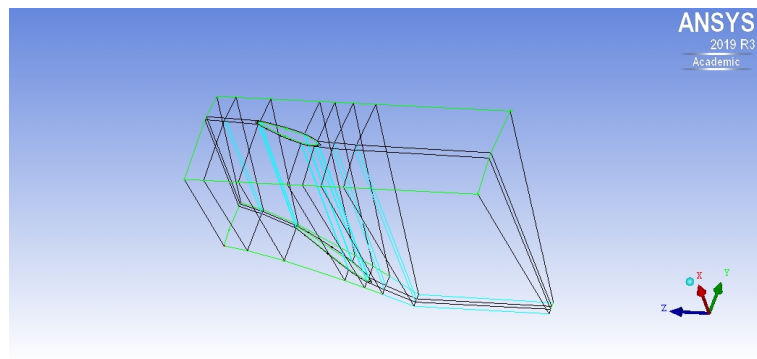


Figure B.6: Blocking of the staggered blade sector

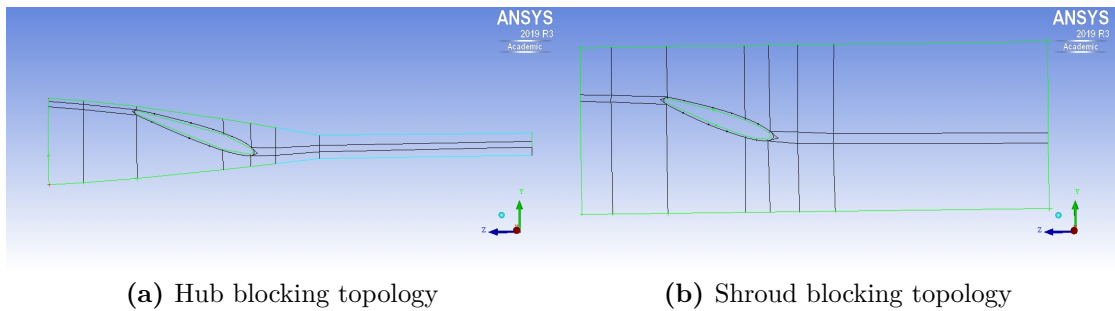


Figure B.7: Block topology details: hub and shroud

heights and ratios: the Y-axis is cumulative distance along the edge, and the X-axis is the number of node points. If there are not enough nodal points to form this linear segment, a hyperbolic law is used and the ratios are ignored. The *Hyperbolic* distribution is calculated automatically by setting *Spacing 1* and *Spacing 2* (the growth ratios are determined internally).

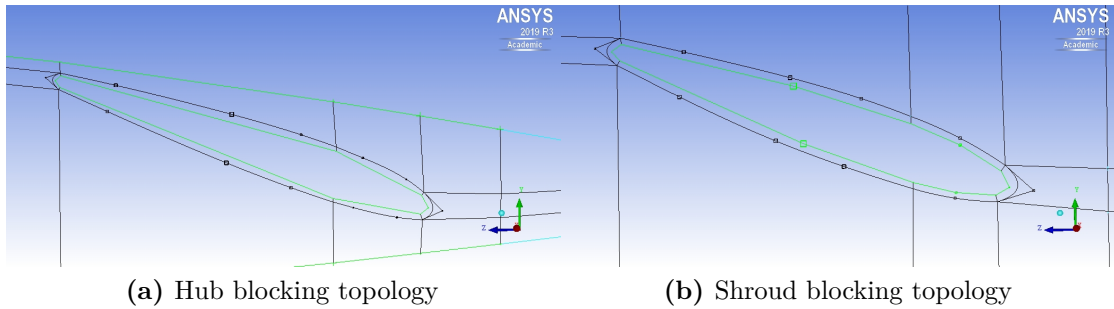


Figure B.8: Block topology details: hub and shroud

- Spacing of the first node from the beginning of the edge (first cell height). When an edge is selected, an arrow appears along the edge. *Spacing 1* refers to the parameters at the beginning end of the arrow, and *Spacing 2* refers to the edge end where the arrow is pointing (Figure B.9). One can also adjust the growth rate from one cell height to the next. *Ratio 1* refers to the parameters at the beginning end of the arrow, and *Ratio 2* refers to the edge end where the arrow is pointing.
- Match spacing between adjacent edges, to have smooth changes from one block to another and no irregularities in the mesh. Regions close to the trailing and leading edge angle, and the wake regions will have denser meshes than the other regions.
- Boundary layer thickness is established following an iterative procedure, as shown later.

The pre-mesh can be visualized after any operation in order to check its quality. The quality can be checked using many different criteria: as shown in Section 2.3.1, there are some precise criteria for the quality of the fluid mesh in CFX. Having all the criteria in the suggested range will help the convergence and produce more accurate and reliable results. The criteria that are carefully checked are:

- Angle: checks the maximum internal angle deviation from 90 degrees for each element. If the elements are distorted and the internal angles are small, the accuracy of the solution will decrease. Internal angles greater than 20° are considered acceptable.
- Aspect Ratio: size of the minimum element edge divided by the size of the maximum element edge. The values are scaled and the default range of values is 1–20, such that an Aspect ratio of 1 indicates a regular element. Double precision should be used for high aspect ratios to get more accurate results.

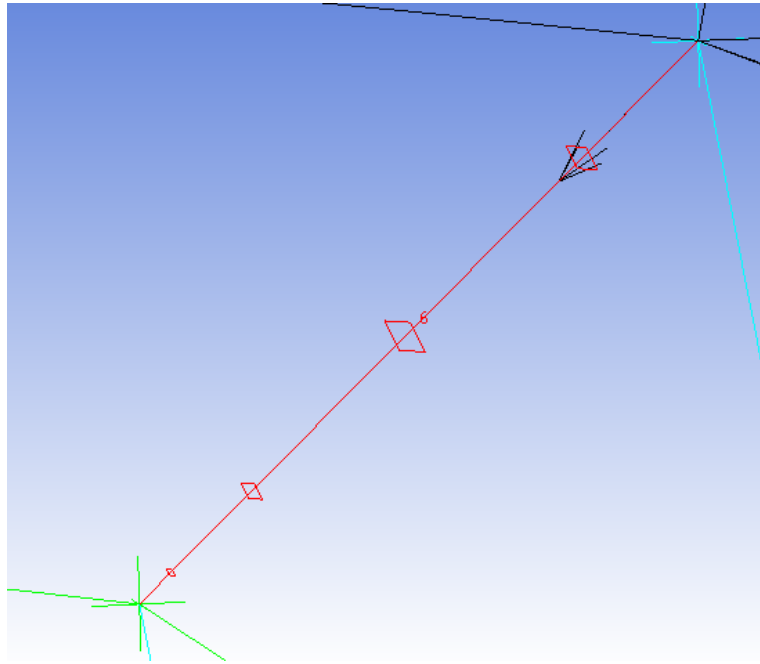


Figure B.9: Example of Edge Spacing with N=6 nodes

In some regions of the boundary layer, aspect ratio can have high values ($10^4 - 10^6$).

- Determinant 3x3x3: Jacobian determinant for hexahedral elements. It should be higher than 0.2-0.3 to be sure that there are no negative volume elements in the mesh (otherwise the simulation in CFX cannot even be started).
- Quality: weighted diagnostic between
 1. Determinant: ratio of the smallest and the largest determinant of the Jacobian matrices, where a Jacobian matrix is computed at each node of the element. Between -1 and 1
 2. Max Orthogls: maximum deviation of the internal angles of the element from 90 degrees. Angles between 180 and 360 degrees (deviation up to 270 degrees) will also be considered.
 3. Max Warppls: maximum warp (distortion) of the faces comprising the element

The minimum of the 3 normalized diagnostics will be used. Quality higher than 0.3 is usually desired.

B.1.3 Iterative Procedure for the y^+ assessment

A correct y^+ value at the boundary layer is fundamental to obtain accurate results. Moreover, the turbulent model is influenced by this value: $k - \varepsilon$ is not reliable at low y^+ (< 11), while $k - \omega$ is good at low y^+ but it loses accuracy in the free turbulence flow (far from the boundary layer region). In this case, low values of y^+ are needed to model the flow correctly: for this reason, an iterative procedure should be applied to find the correct meshing around the BL.

1. Set the number of nodes, spacings (1 and 2) and ratios (1 and 2) around the BL region: the spacing close to the blade curves is the critical one, that will mostly influence the simulations. However, a smooth transition has to be guaranteed and for this reason Ratio 2 is set to 1.2 and all the spacings around the blades are match to make the change as smooth as possible
2. Run a simple SS simulation in CFX with just the IGV
3. Extrapolate the y^+ trend around the blade from the results
4. If $y_{max}^+ > 5$ (or not close to it), go back to the ICEM mesh and decrease the first spacing (eventually increasing the number of nodes in case of overlaps or low quality regions)
5. Iterate this procedure until $y_{max}^+ < 5$ (or at least close to this value)
6. The simulation related to the last iteration is the most accurate and can be used for post processing and further evaluations

For COARSE meshes, even a value $y^+ \approx 5$ is acceptable, while in case of MEDIUM and FINE meshes smaller results can be obtained (around 1-2).

An example of this procedure is illustrated in detail regarding the COARSE mesh. For the other grid sizes, a similar reasoning applies.

- **Iteration 1** (6 nodes in the BL)

- **Reference Blade:** spacing2 = $24 - 55\mu m$ for SHROUD, spacing2 = $25 - 36\mu m$ for HUB.
- **Staggered Blade:** spacing2 = $38 - 58\mu m$ for SHROUD, spacing2 = $27 - 50\mu m$ for HUB.
- y_{max}^+ **after simulation** 33 for the staggered blade and 23 for the other blades

- **Iteration 2** (7 nodes in the BL)

- **Reference Blade:** spacing2 = 3 – 6 μm for SHROUD, spacing2 = 10 – 16 μm for HUB.
- **Staggered Blade:** spacing2 = 2.5 – 3.3 μm for SHROUD, spacing2 = 8 – 22 μm for HUB.
- y_{max}^+ **after simulation** 9.8 for the staggered blade and 7.9 for the other blades

- **Iteration 3** (7 nodes in the BL)

- **Reference Blade:** spacing2 = 3 – 5.9 μm for SHROUD, spacing2 = 2.8 – 5 μm for HUB.
- **Staggered Blade:** spacing2 = 2.5 – 3.3 μm for SHROUD, spacing2 = 1.4 – 3 μm for HUB.
- y_{max}^+ **after simulation** 1.090 for all the blades

The iterative procedure can end after the third iteration. This COARSE mesh is the used to run mesh convergence simulations. Here the information about MEDIUM and FINE mesh after iteration are summarized:

- **MEDIUM** (9 nodes in the BL)

- **Reference Blade:** spacing2 = 0.5 – 1 μm for SHROUD, spacing2 = 0.6 – 1 μm for HUB.
- **Staggered Blade:** spacing2 = 0.8 – 1.1 μm for SHROUD, spacing2 = 0.5 – 1 μm for HUB.
- y_{max}^+ **after simulation** 2.496 for all the blades

- **FINE** (11 nodes in the BL)

- **Reference Blade:** spacing2 = 0.5 – 1 μm for SHROUD, spacing2 = 0.4 – 0.6 μm for HUB.
- **Staggered Blade:** spacing2 = 0.5 – 0.7 μm for SHROUD, spacing2 = 0.5 – 0.9 μm for HUB.
- y_{max}^+ **after simulation** 1.090 for all the blades

B.2 CFX Setup - Grid Dependence Analysis

After loading the mesh (.cfx5 file) in CFX-Pre, the *SOLID* domain can be selected to identify the unique domain (called S1), as shown in Figure B.10. In *Analysis Type*, SS can be chosen. S1 can be initialized by setting *Air Ideal Gas* from the

Material Library, a reference pressure of 0 atm and stationary *domain motion*. Under the voice *Fluid Models*, the turbulence model can be chosen ($k - \varepsilon$, $k - \omega$ or SST). As a next step, the boundaries can be added:

- Blades: *wall* with *no slip wall* properties
- Hub: *wall* with *no slip wall* properties
- Shroud: *wall* with *no slip wall* properties
- Inlet: it can be defined starting from experimental data, i.e. a *.csv* file with total pressure, total temperature, intensity, length scale, Mach number as a function of the blade span. Another option would be to set the value of total pressure to 101325 Pa and total temperature to 288.15 K, and consequently set the turbulence length scale and intensity as a function of the span. It can be shown that the simulation works better in the second case than in the first one, where a value generation starting from the *.csv* file is necessary. Anyway, the experimental *.csv* file is referred to a different inlet area, smaller than the one in the case study. For this reason, a simulation including the rotor is run first (similar to the one in the SS that will be shown in the next sections), and the results are post processed to obtain specific data regarding the inlet and outlet of the IGV. It is important to pay attention to the exact location of the data, since this can cause results that can converge but are wrong in their nature. In this way, the solution converges faster, there is no risk of overflow. Only thing to notice is that a wall is applied to some areas of the Inlet and Outlet sections in order to prevent backflow. This is applied at the beginning of every simulation, and it disappears (or the percentage of the area becomes minimal) after some iterations.
- Outlet: same reasoning than the Inlet section, only difference is that the output file contains information only regarding the average static pressure at the outlet (average over the whole outlet area).
- Periodic Interface: at the extremes of the domain (*2 2D Primitives*). *Rotational periodicity* can be set with *automatic mesh connection* and *direct intersection control*.
- Interfaces between Sectors (4 in total): *2D Primitives* selected as *general connection* between two fluids. *Conservative interface flux* is set and the mesh connection is the same as the periodic interface.

In *Solver Control*, one can set the number of iterations N and the target RMS residual r . In every simulation, $N = 500$ and $r = 10^{-6}$: the simulation stops when the residual is reached. Some monitors for the total pressure at the inlet and outlet

(calculated as mass flow average) can be set as well. Just as an example, in Figures B.11a-B.11b the convergence plot of a simulation (MEDIUM mesh, SST model) is shown after the convergence. As it can be seen, there is a pressure loss from inlet to the outlet, which will be underlined in the next part. In Figures B.12a-B.12b the total pressure decreases as expected towards the outlet (wake generation). The velocity has maximum value at the leading edge of the staggered blade, as expected.

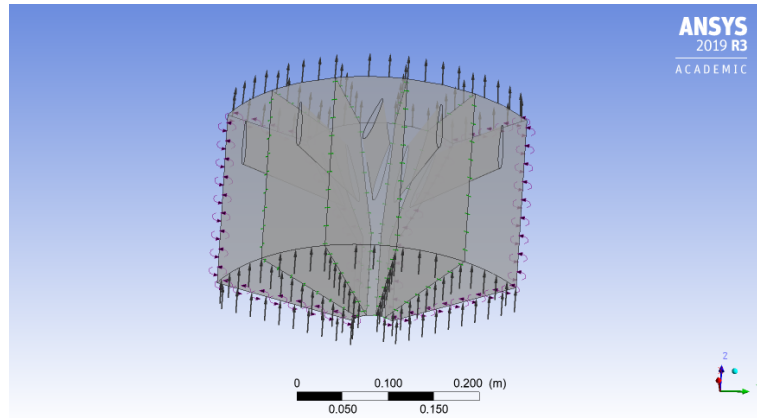


Figure B.10: CFX Setup for grid dependence analysis

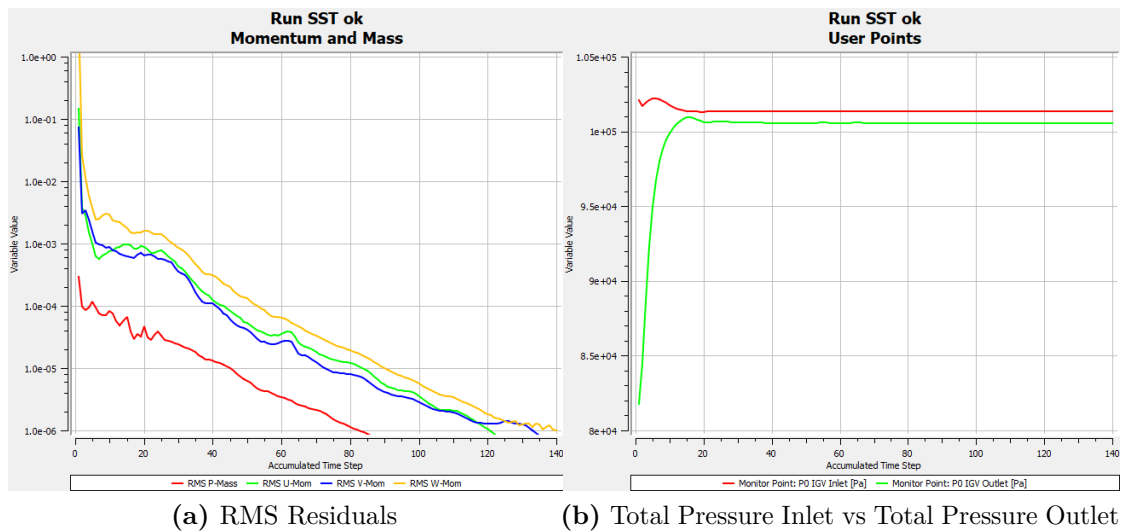


Figure B.11: Residuals and Total pressure monitoring at the end of a simulation - MEDIUM mesh, SST model

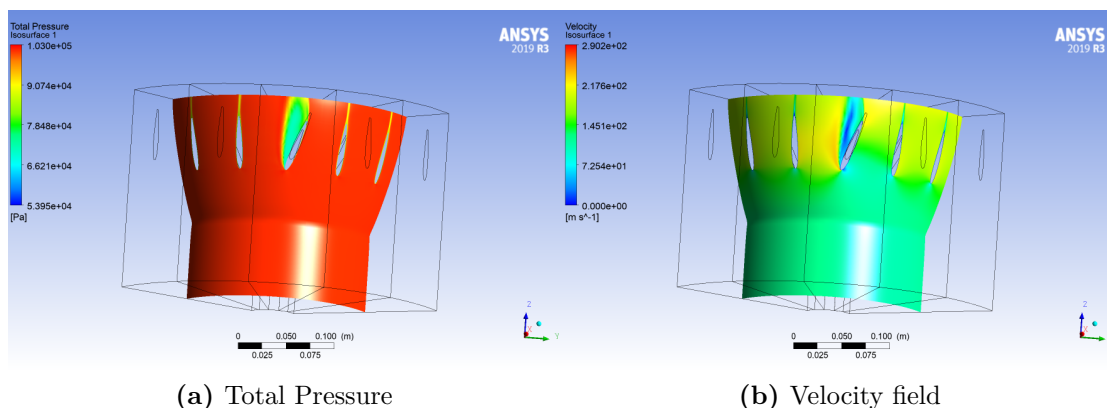


Figure B.12: Trends of total pressure and velocity - MEDIUM mesh, SST model, 50% span

B.3 CFX Setup - SS Simulation

The setup for the IGV is similar to the one done for the grid dependence analysis. At the operating point, the following setup settings are chosen in CFX for rotor, stator and OGV. They are the same in both reference and staggered case.

1. Rotor: rotating at $n = 17185$ rev/min
 - Blade: *wall with no slip wall properties (rotating frame type)*
 - Hub: *wall with no slip wall properties (rotating frame type)*
 - Shroud: *wall with no slip wall properties (rotating frame type with counter rotating wall)*
 - Inflow: *conservative interface flux* between IGV and rotor. The interface is set as *general connection - Stage* and the pitch angles are 24° for the stator side and 22.5° for the rotor.
 - Outflow: *conservative interface flux* between rotor and stator. The interface is set as *general connection - Stage* and the pitch angles are 22.5° for the rotor side and 12.414° for the stator.
 - Periodic Interface: at the extremes of the domain (2D Primitives). *Rotational periodicity* can be set with *automatic mesh connection* and *direct intersection control*
2. Stator: stationary frame
 - Blade: *wall with no slip wall properties (stationary frame type)*

- Hub: *wall with no slip wall* properties (*stationary frame type*)
- Shroud: *wall with no slip wall* properties (*stationary frame type*)
- Inflow: *conservative interface flux* between stator and the rotor. The interface is the same as the interface described for the rotor-stator
- Outflow: *conservative interface flux* between stator and OGV. The interface is set as *general connection - Stage* and the pitch angles are 12.414° 12.414° for the stator side and 72° for the OGV.
- Periodic Interface: at the extremes of the domain (2D Primitives). *Rotational periodicity* can be set with *automatic mesh connection* and *direct intersection control*

3. OGV

- Blade: *wall with no slip wall* properties (*stationary frame type*)
- Hub: *wall with no slip wall* properties (*stationary frame type*)
- Shroud: *wall with no slip wall* properties (*stationary frame type*)
- Inflow: *conservative interface flux* between OGV and stator. The interface is the same as the interface described for the staotr-OGV
- Outflow: the average static pressure is set at 113,000 Pa (*average over the whole outlet*)
- Periodic Interface: at the extremes of the domain (2D Primitives). *Rotational periodicity* can be set with *automatic mesh connection* and *direct intersection control*

Bibliography

- [1] Oddvar Bendiksen. «Review of unsteady transonic aerodynamics: Theory and applications». In: *Progress in Aerospace Sciences* 47 (Feb. 2011), pp. 135–167. DOI: 10.1016/j.paerosci.2010.07.001 (cit. on p. 1).
- [2] Fabian Klausmann and Aaniel Franke. «Lecture 2: TU Darmstadt Transonic Compressor Test Rig». In: *Tech. rep. Technische Universität Darmstadt, Germany* (2020) (cit. on p. 3).
- [3] Ciarán O’Reilly. «Creative Engineers: Is Abductive Reasoning Encouraged enough in Degree Project Work?» In: *Procedia CIRP* 50 (Aug. 2016), pp. 547–552. DOI: 10.1016/j.procir.2016.04.155 (cit. on p. 6).
- [4] Nithin .S and Vijayalakshmi Kovvuri. «REVIEW ON AEROELASTICITY». In: *International Journal of Engineering Applied Sciences and Technology* 04 (Dec. 2019), pp. 271–274. DOI: 10.33564/IJEAST.2019.v04i08.047 (cit. on p. 9).
- [5] Jiří Čečrdle. «Aeroelastic Stability of Turboprop Aircraft: Whirl Flutter». In: Feb. 2018. ISBN: 978-953-51-3807-5. DOI: 10.5772/intechopen.70171 (cit. on p. 10).
- [6] Markus Jöcker, Francois Hillion, Torsten Fransson, and Ulf Wåhlén. «Numerical Unsteady Flow Analysis of a Turbine Stage With Extremely Large Blade Loads». In: vol. 124. June 2001. DOI: 10.1115/2001-GT-0260 (cit. on p. 11).
- [7] Oddvar Bendiksen, Robert Kielb, and Kenneth Hall. «Turbomachinery Aeroelasticity». In: Dec. 2010. ISBN: 9780470686652. DOI: 10.1002/9780470686652.eae156 (cit. on pp. 11, 12, 57, 58).
- [8] Stephen Clark, Robert Kielb, and Kenneth Hall. «Developing a Reduced-Order Model to Understand Non-Synchronous Vibration (NSV) in Turbomachinery». In: vol. 7. June 2012. DOI: 10.1115/GT2012-68145 (cit. on p. 12).
- [9] Mauricio Gutierrez Salas and Carlos Tavera Guerrero. «Lecture 5: Unsteady Aerodynamics Forcing Analysis». In: *Aeromechanics Poject Course, KTH* (2021) (cit. on p. 14).

- [10] ANSYS. *CFX-Solver Modeling Guide, CFX 2019 R3*. 2021 (cit. on pp. 15, 16, 18).
- [11] F. White. *Viscous Fluid Flows, 2nd Edition, McGraw-Hill, New York*. 1991 (cit. on p. 17).
- [12] ANSYS. *CFX-Pre Help*. CFX 2019 R3. 2019 (cit. on pp. 19, 20).
- [13] Haro Correa Elena. «Summer internship TUDA Report». In: (Aug. 2020) (cit. on p. 24).
- [14] Mauricio Gutierrez Salas and Carlos Tavera Guerrero. «Lecture 3: Structural Static Dynamic Analysis». In: *Aeromechanics Poject Course, KTH* (2021) (cit. on p. 43).
- [15] Roberto Biollo and Ernesto Benini. «Recent advances in transonic axial compressor aerodynamics». In: *Progress in Aerospace Sciences* 56 (Jan. 2012). DOI: 10.1016/j.paerosci.2012.05.002 (cit. on p. 58).
- [16] Mario Paz and Young Hoon Kim. *Structural Dynamics: Theory and Computation*. Jan. 2019. ISBN: 978-3-319-94742-6. DOI: 10.1007/978-3-319-94743-3 (cit. on p. 59).
- [17] Alessandro Fasana and Stefano Marchesiello. *Meccanica delle Vibrazioni*. 2006. ISBN: 8879922173 (cit. on pp. 59, 67).
- [18] Hans Martensson, Johan Forsman, and Martin Eriksson. «Simplified Forced Response HCF Assessment of Turbomachinery Blades». In: vol. 6. June 2009, pp. 477–486. DOI: 10.1115/GT2009-60166 (cit. on p. 62).
- [19] Dalila Dimaggio, Andrea Riva, Caterina Bardetta, Andrea Sanguineti, Klaus Störzel, and Sven Käfer. «Fatigue assessment of a notched member under combined LCF and HCF loading». In: *Procedia Structural Integrity* 7 (Jan. 2017), pp. 198–205. DOI: 10.1016/j.prostr.2017.11.078 (cit. on pp. 62, 63).
- [20] Thomas Klauke, Arnold Kühhorn, Bernd Beirow, and Mark Golze. «Numerical Investigations of Localized Vibrations of Mistuned Blade Integrated Disks (Blisks)». In: *Journal of Turbomachinery-transactions of The Asme - J TURBOMACH-T ASME* 131 (July 2009). DOI: 10.1115/1.2985074 (cit. on pp. 63, 64).
- [21] J.F. Wendt, J.D. Jr, Joris Degroote, Gérard Degrez, Erik Dick, R. Grundmann, and J. Vierendeels. *Computational Fluid Dynamics: An Introduction*. Jan. 2009, pp. 1–332. ISBN: 978-3-540-85055-7. DOI: 10.1007/978-3-540-85056-4 (cit. on pp. 67, 68).